
Chapter 14

Radar Cross Section

Eugene F. Knott

Tomorrow's Research

14.1 INTRODUCTION

A radar detects or tracks a target, and sometimes can classify it, only because there is an echo signal. It is, therefore, critical in the design and operation of radars to be able to quantify or otherwise describe the echo, especially in terms of such target characteristics as size, shape, and orientation. For that purpose, the target is ascribed an effective area called the *radar cross section*, or RCS. The RCS is the projected area of a metal sphere that would return the same echo signal as the target, had the sphere been substituted for it.

Unlike the echo of the sphere, however, which is independent of the viewing angle, the echoes of all but the simplest targets vary significantly with orientation. As will be shown later, this variation can be quite rapid, especially for targets many wavelengths in size.

The echo characteristics depend in strong measure on the size and nature of the target surfaces exposed to the radar beam. The variation is small for electrically small targets (targets less than a wavelength or so in size) because the incident wavelength is too long to resolve target details. On the other hand, the flat, singly curved and doubly curved surfaces of electrically large targets all give rise to different echo characteristics. Reentrant structures such as jet engine intakes and exhausts generally have large echoes, and even the trailing edges of airfoils can be significant echo sources.

The radar cross sections of simple bodies can be computed exactly by a solution of the wave equation in a coordinate system for which a constant coordinate coincides with the surface of the body. The exact solution requires that the electric and magnetic fields just inside and just outside the surface satisfy certain conditions that depend on the electromagnetic properties of the material of which the body is made.

While these solutions constitute interesting academic exercises and can, with some study, reveal the nature of the scattering mechanisms that come into play, there are no known tactical targets that fit the solutions. Thus, exact solutions of the wave equation are, at best, guidelines for gauging other (approximate) methods of computing scattered fields.

An alternative approach is the solution of the integral equations governing the distribution of induced fields on target surfaces. The most useful approach to a solution is known as the *method of moments*, in which the integral equations are reduced to a system of linear homogeneous equations. The attraction of this method is that the surface profile of the body is unrestricted, allowing the computation of the scattering

from truly tactical objects. Another is that ordinary methods of solution (matrix inversion and gaussian elimination, for example) may be employed to effect a solution. This method is limited by computer memory and execution time, however, to objects a few dozen wavelengths in size at best.

Alternatives to these exact solutions are several approximate methods that may be applied with reasonable accuracy to electrically large target features. They include the theories of geometrical and physical optics, the geometrical and physical theories of diffraction, and the method of equivalent currents. These approximations are discussed in Section 14.3. Other approximate methods not discussed here are explored in detail in some of the references listed at the end of this chapter.

The practical engineer cannot rely entirely on predictions and computations, and must eventually measure the echo characteristics of some targets. This may be done by using full-scale test objects or scale models thereof. Small targets often may be measured indoors, but large targets must usually be measured on an outdoor test range. The characteristics of typical indoor and outdoor test facilities are described in Section 14.4.

Control of the echo characteristics of some targets is of vital tactical importance, namely *stealth*. There are only two practical ways of reducing the echo: through shaping and radar absorbers. *Shaping* is the selection or design of surface profiles so that little or no energy is reflected back toward the radar. Because target contours are difficult to change once the target has become a production item, shaping is best implemented in the concept definition stage before production decisions have been made. Radar-absorbing materials actually soak up radar energy, also reducing the energy reflected back to the radar. However, the application of absorbers is always expensive, whether gauged in terms of nonrecurring engineering costs, lifetime maintenance, or reduced mission capabilities. The two methods of echo control are discussed in Section 14.5, and a collection of four stealthy platforms is surveyed there.

Seven Basic Echo Mechanisms. Figure 14.1 illustrates seven basic echo sources that might be found on a typical airborne target. All depend in varying degree on the

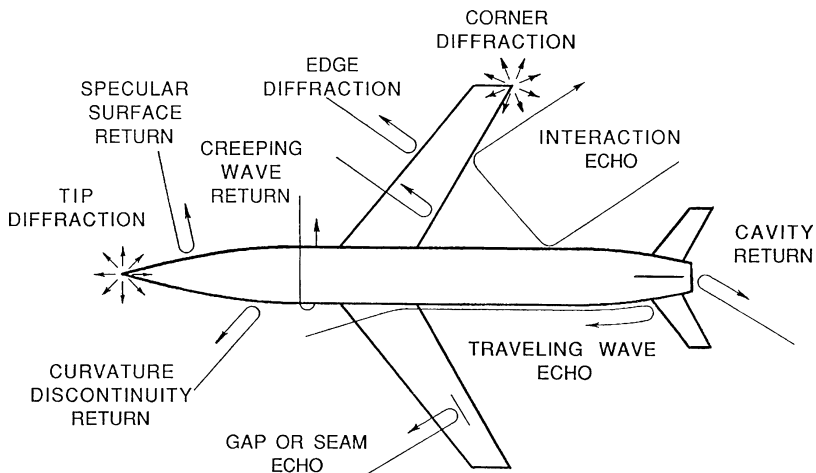


FIGURE 14.1 Examples of seven basic echo-source mechanisms (after E. F. Knott¹ © American Institute of Aeronautics and Astronautics, 1992)

target aspect angle as seen from the radar. Some are dominant scattering mechanisms whereas others are weak. Not all are significant on other kinds of platforms, such as warships or military ground vehicles. We briefly discuss the seven in descending order of significance.

Reentrant Structures. The only reentrant structure appearing on the hypothetical missile in Figure 14.1 is its exhaust duct at the rear, but jet intake ducts behave much the same way. The echoes from cavities such as intake ducts, exhaust ducts, and cockpits are large and tend to persist over aspect angles as wide as 45° or 60° . This is because most of the internal duct surfaces (i.e., compressor stages and turbine faces) are metallic, and any radar wave that finds its way into the structure will likely find its way back out toward the radar. This is also true of internal reflections from within cockpit canopies.

Specular Scatterers. A specular scatterer is any target surface that is oriented perpendicular to the line of sight to the radar. Flat surfaces offer particularly large echoes in the specular direction, but the echoes drop off sharply away from that direction. The specular echoes from singly and doubly curved surfaces (cylindrical and spheroidal surfaces) are somewhat lower than those from flat surfaces, but are more persistent with changes in aspect angle.

Traveling-wave Echoes. When the angle of incidence is a small grazing angle off the surface, a surface traveling wave can be induced. The surface wave tends to build up toward the rear of the body and is usually reflected back toward the front by any discontinuity at the rear. Traveling-wave echoes at low grazing angles are nearly as significant as specular echoes at normal incidence.

Tip, Edge, and Corner Diffraction. Scattering from tips, edges, and corners is less significant than specular echoes and thus are worrisome to the designer only when most other sources of echo have been suppressed. The echoes from tips and corners are localized and tend to increase with the square of the wavelength, not the size of any surface feature. Thus, they become progressively less important as the radar frequency rises.

Surface Discontinuities. Most airframes have slots or gaps where control surfaces meet the stationary airframe. Slots, gaps, and even rivet heads can reflect energy back to the radar. Because these tend to be small effects, it is not easy to isolate and characterize them.

Creeping Waves. A creeping wave is one that gets bound to a smooth, shaded surface, is guided around the rear of a smooth body, and is then launched back to the radar when it reappears at the shadow boundary on the opposite side. As shown in the next section, the creeping wave causes the echoes from small spheres to vary with sphere size. The mechanism can also be present for other smooth bodies, such as the generic missile depicted in Figure 14.1. The creeping wave mechanism is never a significant one for military and civilian targets.

Interactions. Relatively strong echoes can occur when a pair of target surfaces are oriented for a favorable bounce from one surface to another and then back to the radar, as in the interaction between the fuselage and the trailing edge of the right wing shown

in Figure 14.1. Similar interactions occur for ship targets when bulkheads, railings, masts, and other topside features become mirrored in the mean sea surface.

Not all of these mechanisms are revealed in the characteristics of the selection of simple and complex targets, as shown in the next section.

14.2 THE CONCEPT OF ECHO POWER

Definition of RCS. An object exposed to an electromagnetic wave disperses incident energy in all directions. This spatial distribution of energy is called *scattering*, and the object itself is often called a *scatterer*. The energy scattered back to the source of the wave (called *backscattering*) constitutes the *radar echo* of the object. The intensity of the echo is described explicitly by the radar cross section of the object, for which the acronym *RCS* has been generally recognized. Early papers on the subject called it the *echo area* or the *effective area*, terms still found occasionally in contemporary technical literature.

The formal definition of radar cross section is

$$\sigma = \lim_{R \rightarrow \infty} 4\pi R^2 \frac{|E_s|^2}{|E_0|^2} \quad (14.1)$$

where E_0 is the electric-field strength of the incident wave impinging on the target and E_s is the electric-field strength of the scattered wave at the radar. The derivation of the expression assumes that a target extracts power from an incident wave and then radiates that power uniformly in all directions. Although the vast majority of targets do *not* scatter energy uniformly in all directions, the definition assumes that they do. This permits one to calculate the scattered power density on the surface of a large sphere of radius R centered on the scattering object. R is typically taken to be the range from the radar to the target.

The symbol σ has been widely accepted as the designation for the RCS of an object, although this was not so at first.^{2,3} The RCS is the projected area of a metal sphere that is large compared with the wavelength and that, if substituted for the object, would scatter identically the same power back to the radar. However, the RCS of all but the simplest scatterers fluctuates greatly with the orientation of the object, so the notion of an equivalent sphere is not very useful.

The limiting process in Eq. 14.1 is not always an absolute requirement. In both measurement and analysis, the radar receiver and transmitter are usually taken to be in the far field of the target (discussed in Section 14.4), and at that distance, the scattered field E_s decays inversely with the distance R . Thus, the R^2 term in the numerator of Eq. 14.1 is canceled by an identical but implicit R^2 term in the denominator. Consequently, the dependence of the RCS on R , and the need to form the limit, usually disappears.

The radar cross section is, therefore, a comparison of the scattered power density at the receiver with the incident power density at the target. An equally valid definition of the RCS results when the electric-field strengths in Eq. 14.1 are replaced with the incident and scattered magnetic-field strengths. It is often necessary to measure or calculate the power scattered in some other direction than back to the transmitter, a *bistatic* situation. A bistatic RCS may be defined for this case as well as for backscattering, provided it is understood that the distance R is measured from the target to the receiver.

Forward scattering is a special case of bistatic scattering in which the bistatic angle is 180° whence the direction of interest is along the shadow zone behind the target.

The shadow itself can be regarded as the sum of two fields of nearly equal strength but 180° out of phase. One is the incident field, and the other is the scattered field. The formation of the shadow implies that the forward scattering is large, which is indeed the case. The fields behind the target are hardly ever precisely zero, however, because some energy usually leaks into the shadow zone via diffraction from the sides of the target.

Examples of RCS Characteristics. The discussion of radar cross section characteristics will first consider simple targets, of which the sphere is a classic example. This will be followed by complex objects, of which an aircraft is a good example.

Simple Objects. Because of its pure radial symmetry, the perfectly conducting sphere is the simplest of all three-dimensional scatterers. Despite the simplicity of its geometrical surface, however, and the invariance of its echo with orientation, the RCS of the sphere varies considerably with electrical size. The exact solution for the scattering by a conducting sphere is known as the Mie series⁴ and is shown in Figure 14.2.

Note that the chart is split roughly into three regions. In the *Rayleigh region* below $ka < 1$, the RCS rises with the fourth power of the sphere radius, an echo dependence characteristic of electrically small bodies, whether spherical or not. In this region, the incident wave cannot accurately resolve body length-to-width variations. In the optics region above $ka > 10$, optics formulas for predicting the RCS of the metal body generally work reasonably well. Sandwiched between the Raleigh region below and the optics region above is the resonance region, where two or more mechanisms may combine in and out of phase with each other to produce the undulations in the RCS.

In the case of the sphere, the undulations in the resonance region are due to two distinct contributions to the echo, one a *specular reflection* from the front of the sphere and the other a *creeping wave* that circles around its shadowed side. The two go in and out of phase as the sphere grows larger because the difference in the lengths of their electrical path from source to receiver increases continuously with increasing ka . The undulations become weaker with increasing ka because the creeping wave loses more energy the longer the electrical path around the shadowed side.

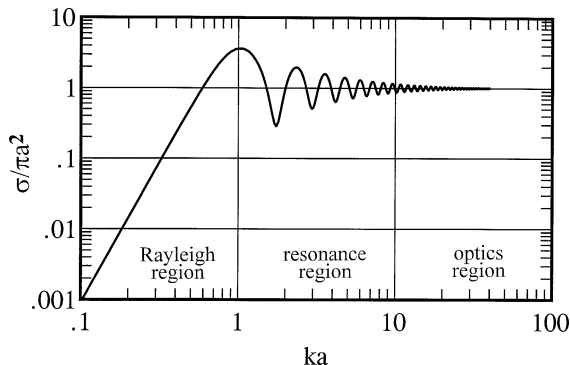


FIGURE 14.2 Radar cross section of a perfectly conducting sphere normalized to the optics value πa^2 . The parameter $ka = 2\pi a/\lambda$ is the circumference of the sphere expressed in wavelengths.

If only the specular reflection is significant, the optics-region RCS of the perfectly conducting sphere is simply

$$\sigma = \pi a^2 \quad (14.2)$$

where a is the radius of the sphere. But the RCS of permeable (dielectric) bodies is more complicated than this because energy can enter the body and rattle around inside before coming back out. An example is the dielectric sphere whose RCS is plotted in Figure 14.3. Because the dielectric material is slightly lossy, as indicated by the non-zero imaginary component of the index of refraction, the RCS of the sphere decays gradually with increasing electrical size. Atlas et al. went even further by comparing the measured and theoretical RCS of Plexiglas spheres in their attempts to understand the scattering by hailstones.⁶

The RCS of very slender dielectric bodies does not exhibit this complexity, however, because the sources of reflection (front and back sides of a dielectric cylinder, for example) are too close to each other to be resolvable by the incident wave. An example is the broadside RCS of a thin string shown in Figure 14.4. The string was angled 45° across the test zone of a large indoor test chamber, and the RCS was measured as a function of frequency for four transmit-receive polarization combinations. Only the copolarized VV and cross-polarized VH traces are shown because the HH and HV measurements closely track the VV and VH data. The measured data are the rapidly varying traces and were fitted statistically to the smoothly varying traces representing the exact solution of the two-dimensional wave equation for dielectric cylinders.

The string diameter was 0.012 inch and its illuminated length was estimated to be about 37 ft. Based on a mean separation between the measured VV and VH data of 10.7 dB, the effective dielectric constant of the string was estimated to be $\epsilon_r = 2.646$. This may be the first time that RCS measurements were ever used to estimate the dielectric constant of a string. Strings are of interest at RCS test facilities because they sometimes are used as “invisible” target supports.

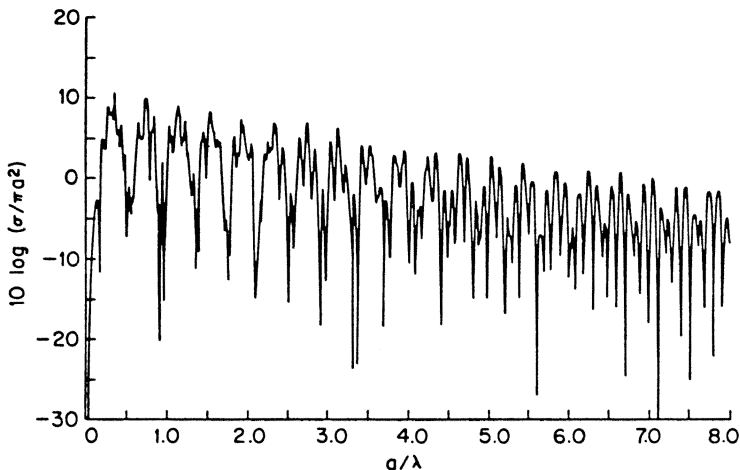


FIGURE 14.3 RCS of a lossy dielectric sphere with $n = 2.5 + i0.01$ (after J. Rheinlein⁵
© IEEE 1968)

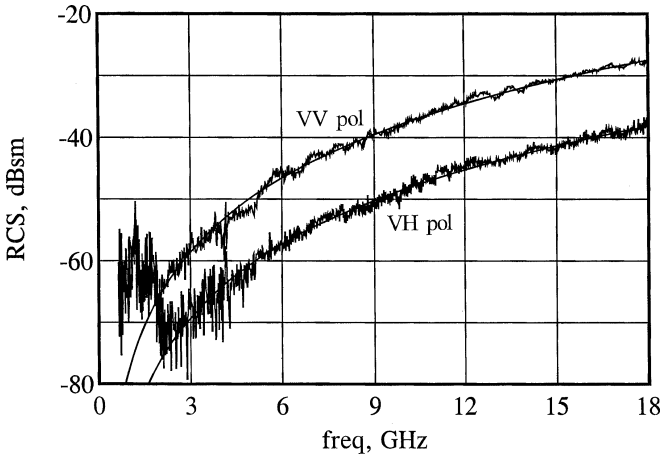


FIGURE 14.4 Measured and predicted broadside RCS of a string stretched across the test zone of an indoor test chamber at 45° angle (© 1999 Horizon House.⁷ Reprinted with permission.)

The behavior of short wire dipoles is markedly different from that of long dielectric strings. As shown in Figure 14.5, the broadside echo of a metal wire exhibits resonances at odd multiples of a half wavelength, with plateaus of nearly constant return between the resonant peaks. These plateaus rise with increasing dipole length and become less distinct as the dipole becomes thicker and longer. They eventually disappear when the dipole becomes fat enough and long enough.

The RCS can rise to significant levels at end-on aspects, as well as in the broadside regions, of bodies both fat and thin. These near-end-on echoes are attributable to surface traveling waves that radiate power in the backward direction. An example is the ogive, a spindle-shaped object formed by rotating an arc of a circle about its chord.

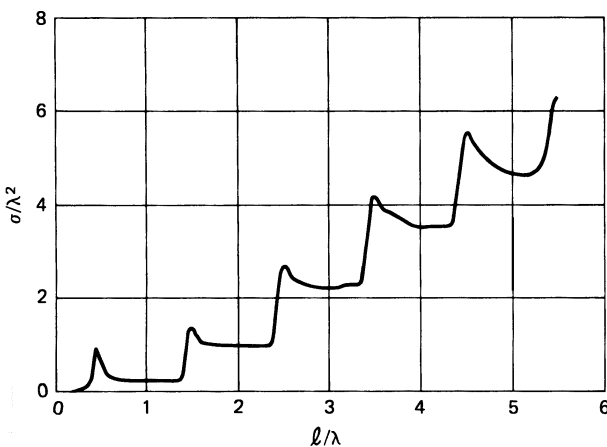


FIGURE 14.5 Measured broadside returns of a thin dipole (Courtesy of University of Michigan Radiation Laboratory⁸)

Figure 14.6 is the RCS pattern of a 39λ long, 15° half-angle ogive recorded for horizontal polarization (incident electric field in the plane of the ogive axis and the line of sight). The large lobe at the right side of the pattern is a specular echo in the broadside sector, and the sequence of peaks at the left side is the contribution of the surface traveling wave near end-on incidence. Note that the RCS is extremely small (not measurable in this case) at precisely end-on incidence. Theoretical predictions in the end-on region closely match the measured pattern for this particular body.

A metal plate is a more elementary structure than the ogive shown in Figure 14.6, but its RCS pattern is no less complex. Sample patterns are reproduced in Figure 14.7 for four different incident and received polarization combinations. The traces for HH (dots) and HV (short dashes) are each shifted down by 5 dB for clarity, whereas those for the VV (long dashes) and VH (solid) are “as is” (not shifted). The plate was rotated about a vertical axis parallel to one edge of the plate, and the incident or received polarization was either parallel to (V) or perpendicular to (H) that axis, respectively.

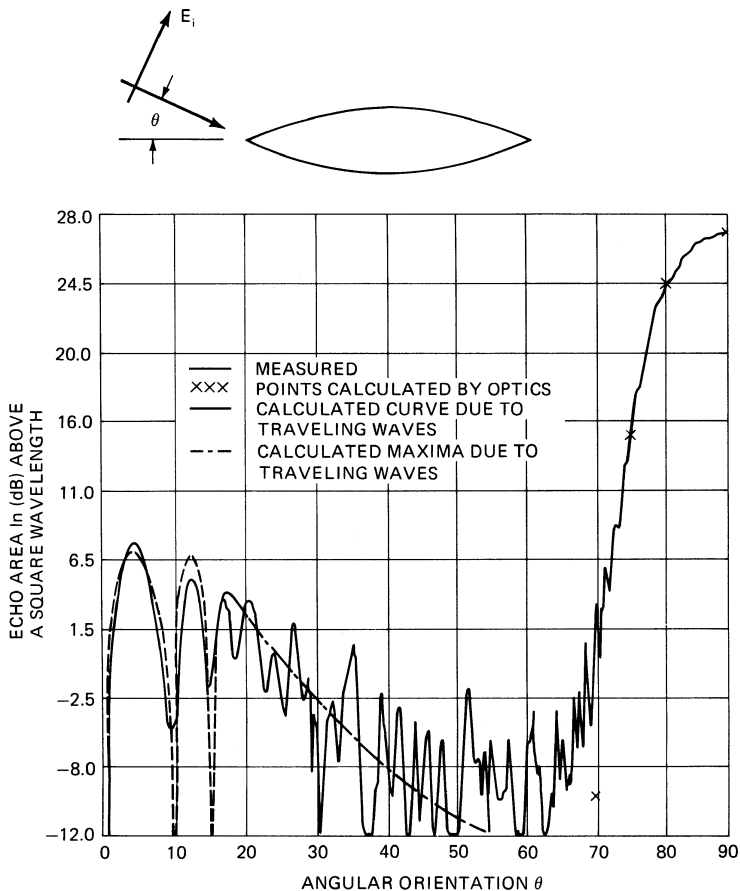


FIGURE 14.6 Measured RCS pattern of a 39λ , 15° half-angle metal ogive (after L. Peters⁹ © IEEE 1958)

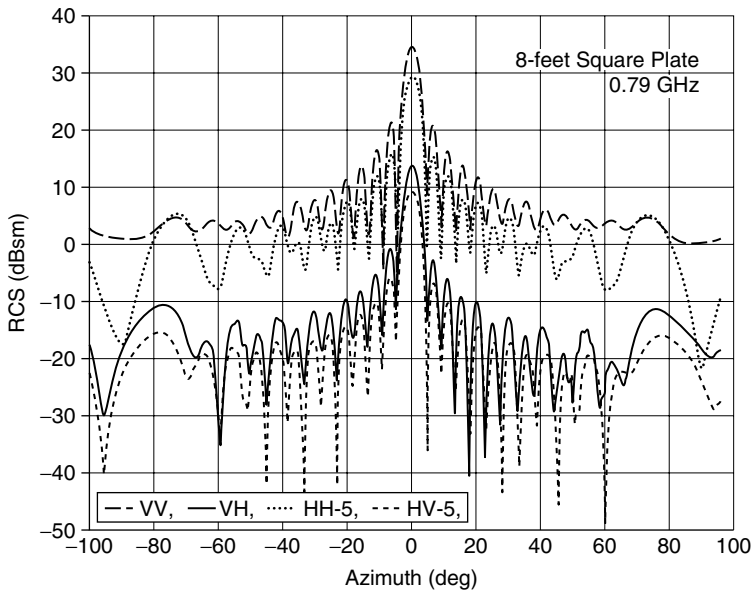


FIGURE 14.7 RCS of a square flat plate 96-in along a side measured at 790 MHz.¹⁰ The HH and HV patterns have been artificially lowered 5 dB for clarity. (Courtesy of S. P. Wei et al.¹⁰, the Boeing Company. Original data courtesy of the Boeing Company, Seattle, Washington.)

The plate is presented broadside to the incident wave at the center of the chart (0°) and is seen edge-on at the left and right sides (90°). The large specular return from the plate at the center of the chart is predicted with quite good accuracy by the flat-plate formula given in Table 14.1, later in this section. The edge-on return for VV polarization is well predicted by the straight-edge formula, also given in Table 14.1.

These undulating plate patterns follow a $\sin x/x$ variation quite closely for aspect angles out to about 30° . Beyond that angle, the two patterns differ by progressively wider margins. The $\sin x/x$ behavior is characteristic of a uniformly illuminated aperture, but unlike the one-way illumination function encountered in antenna work, the argument x for the flat plate includes a two-way (round-trip) illumination function. Thus, the beamwidth of the echo response of a flat plate is half the beamwidth of an antenna aperture of the same size. The prominent lobe in the horizontal pattern in the region between 70° and 80° is due to a surface traveling wave.

In contrast to the pattern of a flat plate, the RCS pattern of a corner reflector is quite broad. This is because the corner reflector is a reentrant structure, and no matter what its orientation (within limits, of course), internally reflected waves are directed back toward the source of the incident wave. A corner reflector is formed by two or three flat plates intersecting at right angles, and waves impinging on the first face are reflected onto the second; if there is a third face, it receives waves reflected by the first two faces. The mutual orthogonality of the faces ensures that the direction taken by waves upon final reflection is back toward the source.

The individual faces of the corner reflector may be of arbitrary shape, but the most common is an isosceles triangle for the trihedral corner; dihedral corners typically have rectangular faces. The RCS of a corner reflector seen along its axis of symmetry

TABLE 14.1 RCS Approximations for Simple Scattering Features

Scattering Feature	Orientation (1)	Approximate RCS	Notes
Corner reflector	Axis of symmetry along LOS	$4\pi A_{\text{eff}}^2/\lambda^2$	(2)
Flat plate	Surface perpendicular to LOS	$4\pi A^2/\lambda^2$	(3)
Singly curved surface	Surface perpendicular to LOS	$2\pi aL^2/\lambda$	(4)
Doubly curved surface	Surface perpendicular to LOS	$\pi a_1 a_2$	(5)
Straight plate edge	LOS perpendicular to front edge and E in plane of plate	L^2/π	(6)
Curved edge	Edge element perpendicular to LOS	$a\lambda/2$	(7)
Cone tip	Axial incidence	$\lambda^2 \sin^4(\alpha/2)$	(8)
Acute flat metal corner	LOS perpendicular to rear edge and E in plane of plate	$(\lambda/6)^2$	(9)
Acute flat metal corner	LOS along corner bisector and E in plane of plate	$(\lambda/40)^2$	(9)

NOTES:

1. LOS = line of sight
2. A_{eff} = effective area contributing to multiple internal reflections
3. A = actual area of the plate
4. a = mean radius of curvature; L = length of slanted surface
5. a_1, a_2 = principal radii of surface curvature in orthogonal planes
6. L = edge length
7. a = radius of edge contour
8. α = half angle of the cone
9. Empirical values reported by Knott, Shaeffer, and Tuley¹⁴

is identical to that of a flat plate whose physical area matches the effective area of the corner reflector. The magnitude of the echo may be determined by finding the polygonal areas on each face of the corner receiving waves reflected by the other faces and from which the final reflection is back toward the source. The effective area is determined by summing the projections of the areas of those polygons on the line of sight¹¹; the RCS is then found by squaring that area, multiplying by 4π , and dividing by λ^2 .

Figure 14.8 is a collection of RCS patterns of a trihedral corner reflector with triangular faces. The reflector was fabricated of three triangular plywood panels, metallized to enhance their surface reflectivities. The aperture exposed to the radar was, therefore, an equilateral triangle, as shown in Figure 14.9. The eight patterns in Figure 14.8 were measured with the plane of the aperture tilted above or below the line of sight by the angle ϕ .

The broad central part of these patterns is due to a triple-bounce mechanism between the three participating faces, while the “ears” at the sides of the patterns are due to the single-bounce, flat-plate scattering from the individual faces. Along the axis of symmetry of the trihedral reflector in Figure 14.9 ($\theta = 0^\circ$, $\phi = 0^\circ$), the RCS is $\pi L^4/3\lambda^2$, where L is the length of one of the edges of the aperture. Not shown are the echo reductions obtained when the trihedral faces are not perpendicular to each other. Those reductions depend on the size of the faces expressed in wavelengths.^{12,13}

The RCS of most of the simple scattering features discussed in this section may be estimated by using the simple formulas listed in Table 14.1. The RCS of some complicated targets may be estimated by representing the target as a collection of features like those listed in Table 14.1, calculating the individual contributions and then summing the contributions coherently or noncoherently, as governed by the objective of the calculations.

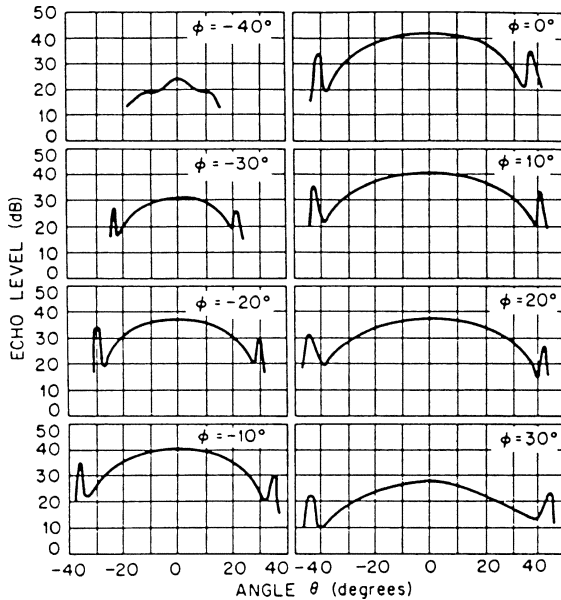


FIGURE 14.8 RCS patterns of a trihedral corner reflector. Edge of aperture = 24 in; $\lambda = 1.25$ cm. (S. S. Robertson³ © AT&T 1947. Reprinted with permission from AT&T Technical Journal.)

Complex Objects. Objects such as insects, birds, airplanes, ships, and antennas can be much more complex than those just discussed, either because of the multiplicity of scatterers on them or because of the complexity of their surface profiles and dielectric constants. Insects are examples of the latter.

Measured values for a dozen species of insects are listed in Table 14.2. The bugs were alive for the measurements but had to be drugged to immobilize them. Figure 14.10 shows the relationship between the RCS and the mass of an insect, with the variation of a water droplet shown for comparison. Table 14.3 lists the RCS of a man as reported by Schultz et al.¹⁶ Other comparisons have been made for both birds and insects.¹⁷

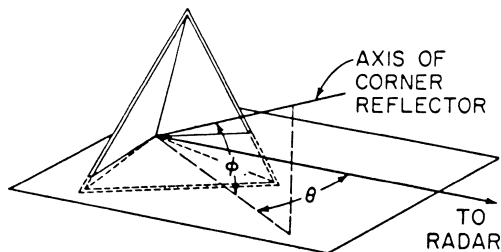


FIGURE 14.9 Coordinate system for the RCS patterns in Figure 14.8. (S. S. Robertson³ © AT&T 1947. Reprinted with permission from AT&T Technical Journal.)

TABLE 14.2 Measured Insect RCS at 9.4 GHz¹⁵

Insect	Length, mm	Width, mm	Broadside RCS, dBsm	End-on RCS, dBsm
Blue-winged locust	20	4	-30	-40
Armyworm moth	14	4	-39	-49
Alfalfa caterpillar butterfly	14	1.5	-42	-57
Honeybee worker	13	6	-40	-45
California harvester ant	13	6	-54	-57
Range crane fly	13	1	-45	-57
Green bottle fly	9	3	-46	-50
Twelve-spotted cucumber beetle	8	4	-49	-53
Convergent lady beetle	5	3	-57	-60
Spider (unidentified)	5	3.5	-50	-52

NOTE: Original values reported in square centimeters have been converted here to dBsm, which is decibels relative to a square meter.

TABLE 14.3 Measured RCS of a Man¹⁶

Frequency, GHz	RCS, m ²
0.41	0.033–2.33
1.12	0.098–0.997
2.89	0.140–1.05
4.80	0.368–1.88
9.375	0.495–1.22

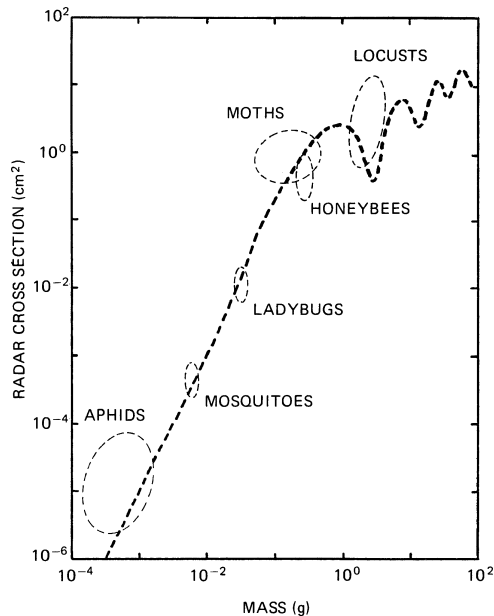


FIGURE 14.10 Sample of measured RCS of insects as a function of insect mass at 9.4 GHz, based on Riley's summary. The dashed line is the calculated RCS of water droplets for comparison. (after J. R. Riley¹⁸ © IEEE 1985)

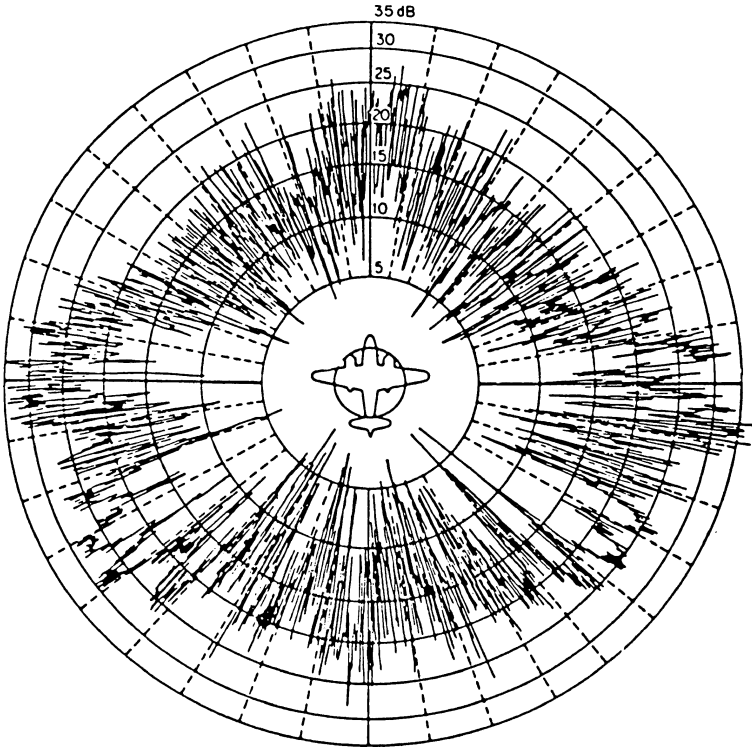


FIGURE 14.11 Measured RCS pattern of a B-26 bomber at a frequency of 3 GHz¹⁹

Examples of RCS patterns for aircraft are shown in Figures 14.11 and 14.12. The B-26 pattern in Figure 14.11 was measured at a frequency of 3 GHz. The polar format is useful for display purposes but is not as convenient for detailed comparisons as is a rectangular format like the one used in Figure 14.12. That rectangular pattern is of a one-third scale model C-29 aircraft and was displayed in the early 2000s on a U.S. Air Force web site.²⁰ The C-29 is a military version of the Raytheon Hawker 800XP mid-size business jet.

The Air Force web site reveals very little technical detail about the test conditions attending the data collection, such as the frequency and polarization of the measurements, not even the units in which the RCS data are displayed. However, even if we do not know the test frequency or polarization, we do know that the full-scale RCS will be $10 \log (3 \times 3) = 9.5$ dB higher than those charted in the figure (i.e., higher by the square of the inverse scale factor). We suspect that nose-on incidence is at the center of the pattern and that the charted RCS data are in decibels above a square meter at the test frequency.

Figure 14.13 charts the RCS of a ship measured at 2.8 and 9.225 GHz at horizontal polarization. The data were collected by a shore-based radar instrumentation complex as the ship steamed in a large circle on Chesapeake Bay. The three traces in these charts are the 80, 50, and 20 percentile levels of the signals collected over aspect angle “windows” 2° wide. The patterns are not symmetrical, especially at the higher frequency. Note that the RCS can exceed 1 m^2 (64.1 dBsm).

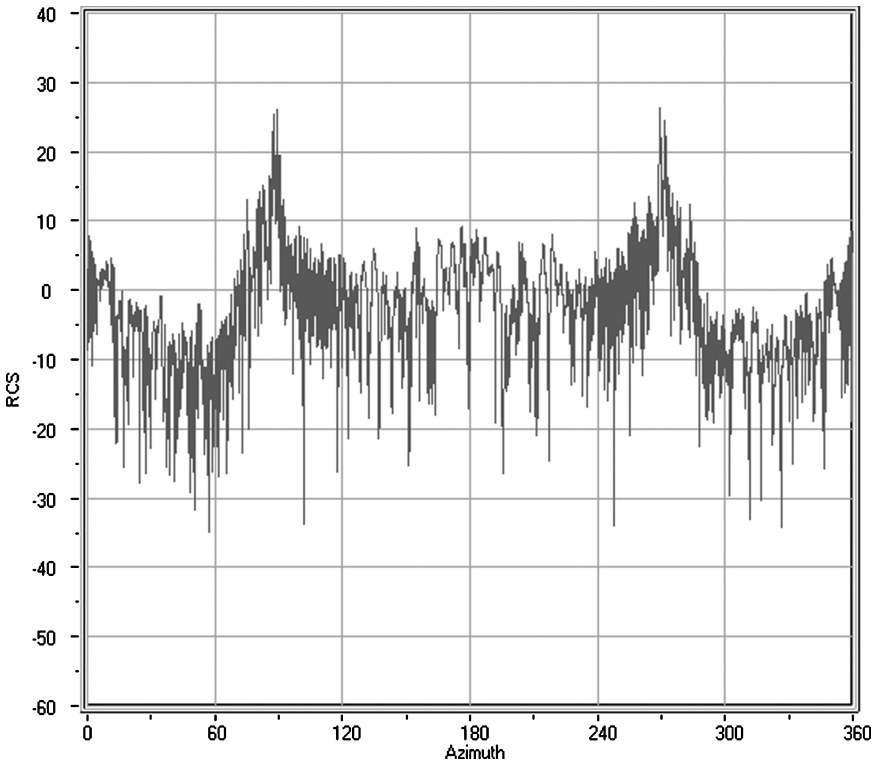


FIGURE 14.12 Measured RCS of a one-third scale model C-29 military aircraft²⁰

An empirical formula for the RCS of a naval ship is

$$\sigma = 52 f^{1/2} D^{3/2} \quad (14.3)$$

where f is the radar frequency in megahertz and D is the full-load displacement of the vessel in kilotons.^{21,22} The relationship is based on measurements of several ships at low grazing angles and represents the average of the median RCS in the port and starboard bow and quarter aspects, but excluding the broadside peaks. The statistics include data collected at nominal wavelengths of 3.25, 10.7, and 23 cm for ship displacements ranging from 2 to 17 kilotons.

Figure 14.14 summarizes the general RCS levels of the wide variety of targets discussed in this section, with the RCS of a metallic sphere shown as a function of its volume for comparison. The ordinate is the RCS in square meters, and the abscissa is the volume of the target in cubic feet. Because the chart is intended only to display the wide range in RCS that may be encountered in practice, the locations of targets on the chart are approximate at best. Within given target classes, the RCS may be expected to vary by as much as 20 or 30 dB, depending on frequency, aspect angle, and specific target characteristics. Readers seeking more explicit detail than this should consult referenced material at the end of this chapter.

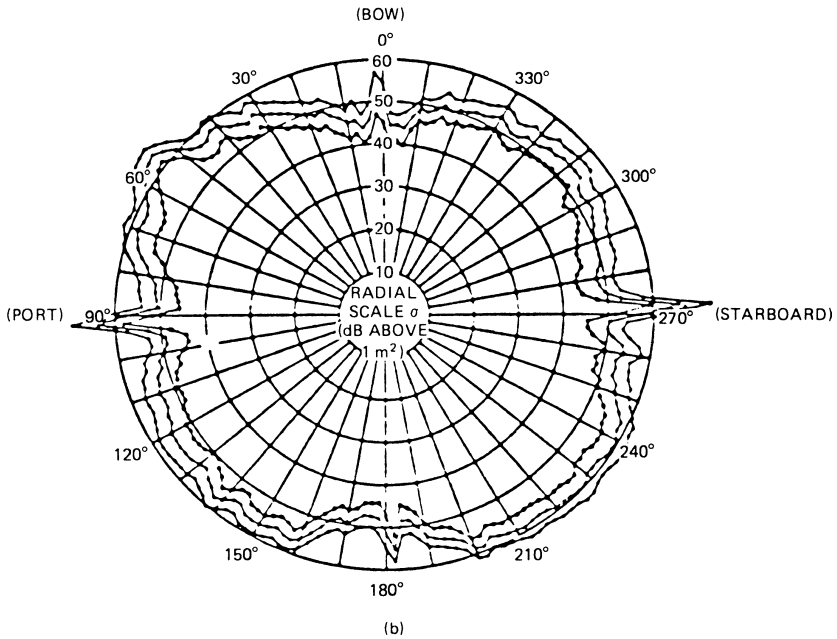
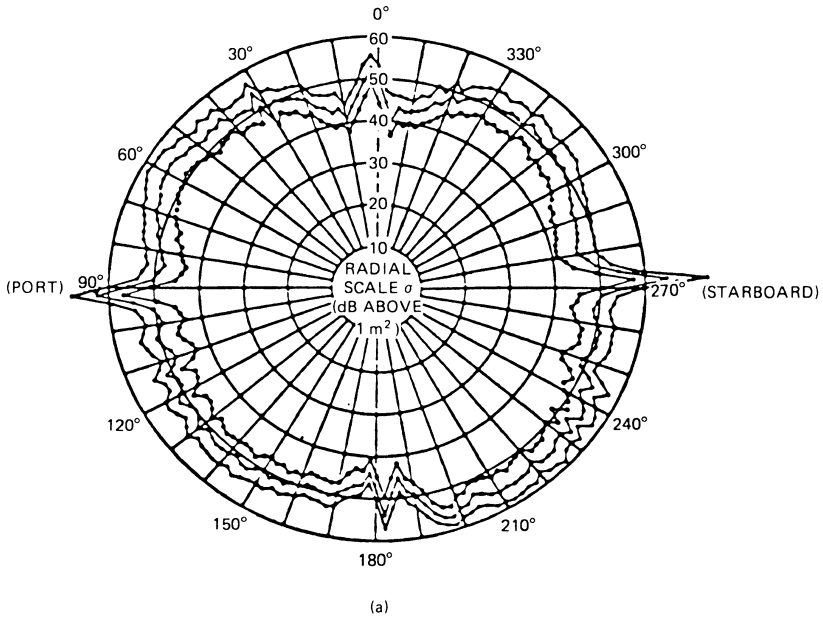


FIGURE 14.13 Measured RCS of a large naval auxiliary ship for horizontal incident polarization. The upper pattern (a) is for 2.800 GHz, and the lower pattern (b) is for 9.225 GHz. Shown are the 80, 50, and 20 percentile levels based on the statistics of the data over 2° aspect angle windows.

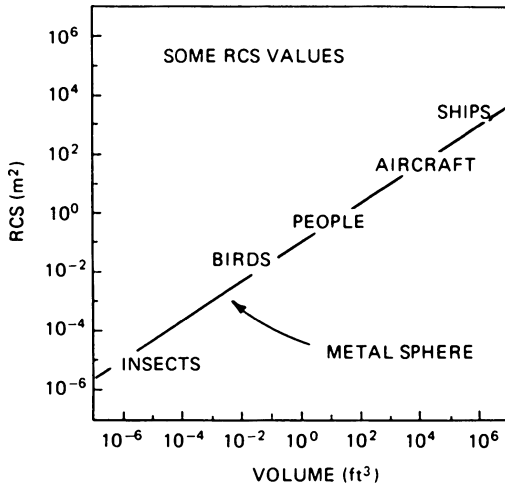


FIGURE 14.14 Summary of RCS levels of targets discussed in this section. The locations of targets on the chart are general indications only.

14.3 RCS PREDICTION TECHNIQUES

As shown in Figure 14.2, scattering obstacles are generally sorted into three different regimes based on their body size in wavelengths. Very loosely, these three regions are

- Rayleigh region: typical body size $< \lambda$
- Resonance region: $\lambda < \text{typical body size} < 3\lambda$
- Optics region: $3\lambda < \text{typical body size}$

The boundaries separating the three regimes are diffuse at best. The utility of our RCS estimation and computation methods depends in large measure on where in this size scheme we find our target.

Although the complexity and size of most scattering objects preclude the application of exact methods of radar cross-section prediction, exact solutions for simple bodies provide valuable checks for approximate methods. The exact methods are restricted to relatively simple or relatively small objects in the Rayleigh and resonant regions, whereas most of the approximate methods have been developed for the optics region, also called the *high-frequency region*. There are exceptions to these general limitations, of course. The exact solutions for many objects can be used for large bodies well into the optics region if one uses arithmetic of sufficient precision, and many optics approximations can be extended to bodies of modest electrical size into the resonance region. Low-frequency approximations developed for the Rayleigh region can extend upward into the resonance region.

Exact Methods. The exact methods are based on either the integral or differential form of Maxwell's equations.

Differential Equations. Maxwell's four differential equations constitute a succinct statement of the relationship between electric and magnetic fields produced by currents and charges and by each other.²³ The four equations may be manipulated for isotropic source-free regions to generate the wave equation:

$$\nabla^2 \mathbf{F} + k^2 \mathbf{F} = 0 \quad (14.4)$$

where \mathbf{F} represents either the vector electric field or the vector magnetic field. Equation 14.4 is a second-order differential equation that may be solved as a boundary-value problem when the fields on the surface of the scattering obstacle are specified. The fields are typically represented as the sum of known and unknown components (incident and scattered fields), and the boundary conditions are the known relationships that must be satisfied between the fields (both electric and magnetic) just inside and just outside the surface of the obstacle. Those boundary conditions are particularly simple for solid conducting or dielectric objects.

The boundary conditions involve all three components of the vector fields, and the surface of the body must coincide with a coordinate of the geometrical system in which the body is described. For example, the coordinate $r = \text{constant}$ could represent a spherical surface. The solution of the wave equation is most useful for those systems in which the equation is separable into ordinary differential equations in each of the variables. The scattered fields are typically expressed in terms of infinite series, the coefficients of which are to be determined in the actual solution of the problem. Once obtained, the solution allows the fields to be calculated at any point in space, which in RCS problems is the limit as the distance from the obstacle becomes infinite. The solution of the wave equation may then be used in Eq. 14.1 to determine the scattering cross section.

Aside from a few very simple objects, such as the sphere and the infinite circular cylinder, the solution for Eq. 14.4 is more academic than practical. The solution for other structures, such as infinite parabolic and elliptic cylinders, are difficult at best, and for many structures whose surfaces may coincide with a coordinate system, there is no convenient method of solution.

The most useful and practical of the exact solutions available is that of the perfectly conducting sphere, shown earlier in Figure 14.2. Metal spheres are used routinely as calibration targets for RCS measurements because an exact solution is available; metal spheres are not very hard to build; and efficient computer codes are available for obtaining the exact solution. No other scattering body affords all these conveniences.

Integral Equations. Maxwell's equations may also be manipulated to generate a pair of integral equations (known as the Stratton-Chu equations²⁴):

$$\mathbf{E}_s = \oint \{ ikZ_0 (\mathbf{n} \times \mathbf{H}) \Psi + (\mathbf{n} \times \mathbf{E}) \times \nabla \Psi + (\mathbf{n} \cdot \mathbf{E}) \nabla \Psi \} dS \quad (14.5)$$

$$\mathbf{H}_s = \oint \{ -ikY_0 (\mathbf{n} \times \mathbf{E}) \Psi + (\mathbf{n} \times \mathbf{H}) \times \nabla \Psi + (\mathbf{n} \cdot \mathbf{H}) \nabla \Psi \} dS \quad (14.6)$$

where \mathbf{n} is the unit surface normal erected at the surface patch dS and Ψ is the Green's function:

$$\Psi = e^{ikr}/4\pi r \quad (14.7)$$

The distance r in Eq. 14.7 is measured from the surface patch dS to the point at which the scattered fields are desired, which could be another surface patch. These expressions state that if the total electric and magnetic field distributions are known over a completely closed surface S (as indicated by the little circle on the integral sign), the fields anywhere in space may be computed by summing (integrating) those surface field distributions over the entire surface. This scattering problem relies on the same two equations, but instead of measuring the total fields over a closed surface surrounding the body, one determines the fields induced on the body surfaces themselves by the incident wave and then solves a system of linear equations. These surface fields become unknowns to be determined. The two equations are coupled because the unknowns appear on both sides of both equations. The method of solution is known as the *method of moments (MOM)*,²⁵ which reduces the integral equations to a collection of homogeneous linear equations that may be solved by matrix techniques.

Once the boundary conditions have been specified, the surface S is split into a collection of discrete patches, as suggested in Figure 14.15. The patches must be small enough (typically less than $\lambda/5$) that the unknown currents and charges over each patch are constant or at least can be described by simple functions. A weighting function may be assigned to each patch, and the problem is essentially solved when the amplitude and phase of those functions have been determined.

If the point of observation is forced down to a general surface patch, the fields on the left sides of Eqs. 14.5 and 14.6 are those due to the contributions of the fields on all other patches, plus the incident fields and a "self-field." The self-field (or self-current or self-charge) is moved to the right side of the equations, leaving only the known incident field on the left side. When the process is repeated for each patch on the surface, a system of $2n$ linear homogeneous equations in $2n$ unknowns is generated. If the boundary conditions permit the decoupling of the equations, the number of unknowns may be halved (to n equations in n unknowns).

The coefficients of the resulting matrix involve only the electrical distances (in wavelengths) between all patches taken by pairs, and the orientation of patch surface normals. The unknown fields may be found by inverting the resulting matrix and multiplying the inverted matrix by a column matrix representing the incident field at each patch. The surface fields are then summed in integrals similar to Eqs. 14.5 and 14.6 to obtain the scattered field, which then may be inserted in Eq. 14.1 to compute the RCS.

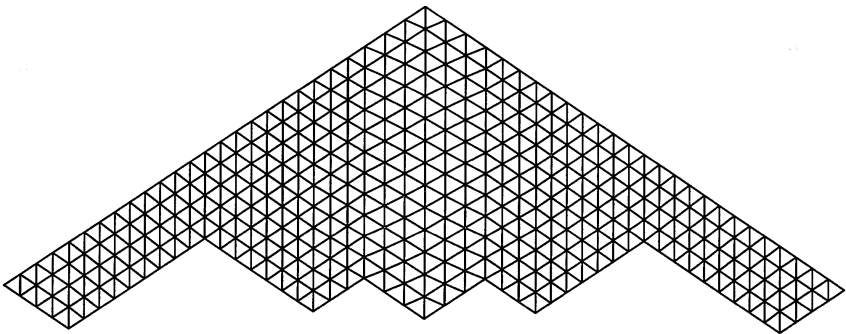


FIGURE 14.15 The method of moments divides the body surface into a collection of discrete patches. This planform of the U.S. Air Force B-2 Spirit stealth bomber uses triangular patches.

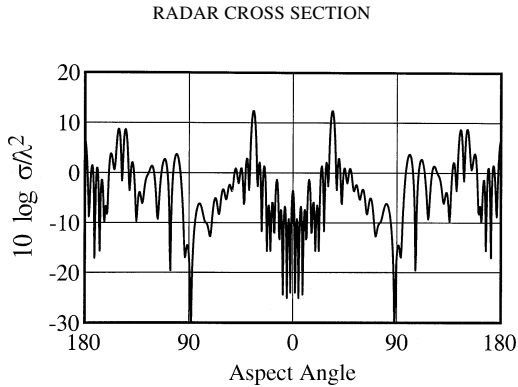


FIGURE 14.16 Azimuth-plane MOM-predicted edge-on RCS of a flat plate having the planform shown in Figure 14.15 for wing leading edges 5λ in length. The incident electric field was in the plane of the plate.

The method of moments has become a powerful tool in the prediction and analysis of electromagnetic scattering, with applications for antenna design as well as RCS prediction. This method has three limitations, however.

First, because computer memory and processing time both increase rapidly with the electrical size of the object, there might be an economic limit for the maximum target electrical size (in wavelengths) for which MOM can be used. Second, MOM yields numbers, not formulas, and is therefore a numerical experimental tool. However, trends may be established by running these numerical experiments repeatedly for parametric changes in the geometry or configuration of an object, or in the angle of arrival or of the frequency, of the incident wave. Third, the solutions for some objects may contain spurious resonances that do not actually exist, thereby reducing the confidence one may have in applying the method to arbitrary structures.

Figure 14.16 shows a MOM-code prediction of the edge-on RCS pattern of a large, flat metal plate of zero thickness having the planform of Figure 14.15. For the purpose of illustration, we chose a simulation frequency such that the leading edges of the wings were 5λ long. The incident polarization and the direction of the incident wave were both in the plane of the plate. Nose-on incidence lies at zero-degree aspect at the center of the chart, and the tail-on aspect lies at 180° at both sides of the chart.

As shown in Table 14.1, the approximate RCS of a straight edge of length L presented perpendicular to the incident wave is $\sigma = L^2/\pi$. However, this estimate is some 3 dB lower than the peak amplitude attained in Figure 14.16 by the leading-edge echoes 34° either side of nose-on incidence. Evidently there are other, more subtle echo sources that contribute to the RCS at these aspects, possibly surface traveling-wave contributions.

Approximate Methods. Approximate methods for computing scattered fields are available in both the Rayleigh and the optics regions. Rayleigh-region approximations may be derived by expanding the wave equation (Eq. 14.4) in a power series of the wavenumber k .²⁶ Higher-order terms of the expansion become progressively more difficult to obtain. The RCS pattern of a Rayleigh scatterer is very broad, especially if the object has similar transverse and longitudinal dimensions. The magnitude of the echo is proportional to the square of the volume of the object and varies as the fourth

power of the frequency of the incident wave.²⁷ Because the method of moments is quite well suited to the solution of Rayleigh-region problems, analytical Rayleigh-region expansions for predicting the RCS of electrically small objects have lapsed into disuse.

Several approximate methods have been devised for the optics region, each with its particular advantages and limitations. The most mature of the methods are *geometric optics* and *physical optics*, with later methods attacking the problem of diffraction from edges and from shadow boundary field discontinuities. While the general accuracy of the optics region approximations improves as the scattering obstacle becomes electrically larger, some of them give reasonably accurate results (within 1 or 2 dB) for objects as small as a wavelength or so.

Geometric Optics. The theory of geometric optics (GO) is based on the conservation of energy within a slender fictitious tube called a *ray*. The direction of propagation is along the tube, and contours of equal phase are perpendicular to it. In a lossless medium, all the energy entering the tube at one end must come out the other end, but energy losses within the medium may also be accounted for. An incident wave may be represented as a collection of a large number of rays, and when a ray strikes a surface, part of the energy is reflected and part is transmitted across the surface. The amplitude and phase of the reflected and transmitted rays depend on the properties of the media on either side of the surface. The reflection is perfect if the surface is perfectly conducting, and no energy is transmitted across the boundary into the body. When energy can pass through the surface, transmitted rays are bent toward the surface normal in crossing a surface into an electrically denser medium (higher index of refraction) and away from the surface normal into a less dense medium. This bending of rays is known as *refraction*.

Depending on surface curvature and body material, reflected and transmitted rays may diverge from one another or they may converge toward each other. This dependence is the basis for the design of lenses and reflectors at radar wavelengths as well as at optical wavelengths. The reduction in intensity as the rays diverge (spread away) from the point of reflection can be calculated from the curvatures of the reflecting surface and the incident wave at the *specular point*, which is that point on the surface where the angle of reflection equals the angle of incidence. The principal radii of curvature of the surface are measured in two orthogonal planes at the specular point, as shown in Figure 14.17. When the incident wave is planar and the direction of interest is back toward the source, the geometric optics RCS is simply

$$\sigma = \pi a_1 a_2 \quad (14.8)$$

where a_1 and a_2 are the radii of curvature of the body surface at the specular point.

This formula becomes exact in the optical limit of vanishing wavelengths and is probably accurate to 10 or 15 percent for radii of curvature as small as 2λ or 3λ . It assumes that the specular point is not close to an edge. When applied to dielectric objects, the expression should be multiplied by the square of the voltage reflection coefficient associated with the material properties of the object. Internal reflections may also be accounted for, and the phase of internally reflected rays should be adjusted according to the electrical path lengths traversed within the body material. The net RCS should then be computed as the coherent sum of the surface reflection plus all significant internal reflections. Equation 14.8 fails when one or both surface radii of

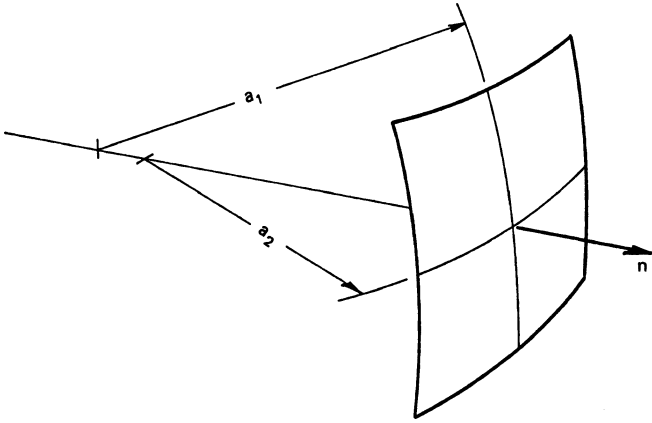


FIGURE 14.17 The geometric optics RCS of a doubly curved surface depends on the principal radii of curvature at the specular point. The specular point is where the surface normal points toward the radar.

curvature at the specular point become infinite, yielding infinite RCS, which is obviously wrong. This occurs for flat and singly curved surfaces.

Physical Optics. The theory of physical optics (PO) is a suitable alternative for bodies with flat and singly curved surface features. The theory is based on two approximations in the application of Eqs. 14.5 and 14.6, both of which are reasonably effective in a host of practical cases. The first is the *far-field approximation*, which assumes that the distance from the scattering obstacle to the point of observation is large compared with any dimension of the obstacle itself. This allows us to replace the gradient of Green's function with

$$\nabla\psi = ik\psi_o\mathbf{s} \quad (14.9)$$

$$\psi_o = e^{-ik\mathbf{r} \times \mathbf{s}} e^{ikR_o}/4\pi R_o \quad (14.10)$$

where \mathbf{r} is the position vector of integration patch dS and \mathbf{s} is a unit vector pointing from an origin in or near the object to the far-field observation point, usually back toward the radar. R_o is the distance from the origin of the object to the far-field observation point.

The second is the *tangent plane approximation*, in which the tangential field components $\mathbf{n} \times \mathbf{E}$ and $\mathbf{n} \times \mathbf{H}$ are approximated by their geometric optics values. That is, a tangent plane is passed through the surface coordinate at the patch dS , and the total surface fields are taken to be precisely those that would have existed had the surface at dS been infinite and perfectly flat. In essence, we do not know these fields, but we take our best guess as to what they are and insert that estimate into either of the two integrals. That done, the estimate of the unknown fields in the integrals of Eqs. 14.5 and 14.6 may be expressed entirely in terms of the known incident field values. The problem then becomes one of evaluating the chosen integral and substituting the result into Eq. 14.1 to obtain the RCS.

If the surface is a good conductor, the total tangential electric field is virtually zero and the total tangential magnetic field is twice the amplitude of the incident tangential magnetic field:

$$\mathbf{n} \times \mathbf{E} = 0 \quad (14.11)$$

$$n \times \mathbf{H} = \begin{cases} 2n \times \mathbf{H}_i & \text{illuminated surfaces} \\ n & \text{shaded surfaces} \end{cases} \quad (14.12)$$

Note that the tangential components of both the electric and the magnetic fields are set to zero over those parts of the surface shaded from the incident field by other body surfaces. Other approximations may be devised for nonconducting surfaces. If the incident wavelength is long enough, for example, the surface of a soap bubble or the leaf of a tree may be modeled as a thin membrane, over which neither the electric nor magnetic fields are zero.

The physical-optics integral is easy to evaluate for flat metallic plates because the phase is the only quantity within the integral that varies, and it varies linearly across the surface. When applied to a rectangular metal plate, the integral evaluation leads to the RCS:

$$\sigma = 4\pi \left| \frac{A \cos \theta}{\lambda} \cdot \frac{\sin(k\ell \sin \theta \cos \phi)}{k\ell \sin \theta \cos \phi} \cdot \frac{\sin(kw \sin \theta \sin \phi)}{kw \sin \theta \sin \phi} \right|^2 \quad (14.13)$$

where $A = \ell w$ is the physical area of the plate, θ is the angle between the surface normal of the plate and the direction to the radar, ϕ is the angle between the plane containing the line of sight and the edge whose length is ℓ , and w is the width of the plate. (A more general physical optics formula is available for the bistatic scattering from any polygonal plate.^{28,29})

If we set $\phi = 0^\circ$ or 90° , we obtain a *principal plane* RCS pattern (incidence in a plane perpendicular to a pair of edges). When $\phi = 0^\circ$, Eq. 14.13 becomes

$$\sigma = 4\pi \left| \frac{A \cos \theta}{\lambda} \cdot \frac{\sin(k\ell \sin \theta)}{k\ell \sin \theta} \right|^2 \quad (14.14)$$

If we set $\phi = 90^\circ$ instead of $\phi = 0^\circ$, we get nearly the same answer, except that $k\ell$ in Eq. 14.14 becomes kw . The physical optics integral is not dependent on the polarization of the incident wave and is unreliable for angles much greater than 30° from broadside incidence.

By way of comparison, the physical optics formula for the RCS of a circular metal disk is

$$\sigma = 16\pi \left| \frac{A \cos \theta}{\lambda} \cdot \frac{J_1(kd \sin \theta)}{kd \sin \theta} \right|^2 \quad (14.15)$$

where A is the physical area of the disk, d is its diameter, and $J_1(x)$ is the Bessel function of the first kind of order 1. Equations 14.13 through 14.15 all reduce to the value listed in Table 14.1 for normal incidence. For further comparison, the PO patterns of two square plates and a circular disk are plotted in Figure 14.18.

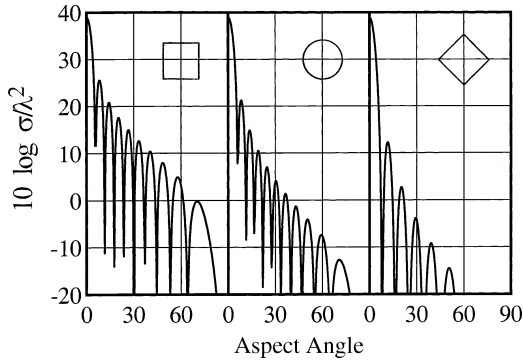


FIGURE 14.18 PO patterns of the RCS of a square plate, a disk, and second square plate

The three patterns each cover a 90° sector from broadside to edge-on and are placed side-by-side for clarity. The areas of all three plates were fixed at $25\lambda^2$, hence all three patterns rise to the same amplitude at broadside incidence (zero aspect). The center pattern is for the disk, while the first and third are both for a square plate. However, the square plate was oriented for a principal-plane pattern in the leftmost chart and like a diamond ($\phi = 45^\circ$) in the rightmost chart. The amount of surface distributed toward the sides of the plates influences the sidelobe levels.

The PO integral is somewhat more complicated to evaluate when the surface is singly or doubly curved. An exact evaluation can be performed for a circular cylinder and a spherical cap viewed along the axis of symmetry, but not for a truncated cone or a spherical cap seen along other than the axis of symmetry. Even so, the exact evaluation for the cylinder includes fictitious contributions from the shadow boundaries at the sides of the cylinder that do not appear in a *stationary phase approximation*.³⁰

The amplitude of the elemental surface contributions changes slowly over the surface of integration whereas the phase changes much more rapidly. As such, the net contribution in regions of rapid phase change is essentially zero and may be ignored. As the specular regions are approached, on the other hand, the phase variation slows down and then reverses as the specular point is crossed. This results in a nonzero specular contribution to the integral. The phase variation near the shadow boundaries is rapid, hence, surface contributions there are ignored in a stationary phase evaluation, but an exact evaluation includes them because the shadow boundaries are the limits of integration. Because the actual surface field distributions do not suddenly drop to zero as the shadow boundary is crossed, as assumed by the theory, the shadow boundary contributions are spurious.^{31,32} Thus, a stationary phase approximation of the physical optics integral over closed curved surfaces tends to be more reliable than an exact evaluation of the integral.

With this in mind, the stationary phase result for a circular cylinder is

$$\sigma = ka\ell^2 \left| \frac{\sin(k\ell \sin \theta)}{k\ell \sin \theta} \right|^2 \quad (14.16)$$

where a is the radius of the cylinder, ℓ is its length, and θ is the angle off broadside incidence. Equation 14.16 includes only the contribution from the curved side of the

cylinder and not its flat ends, which may be included by using the prescription of Eq. 14.15. Equation 14.16 may also be used to estimate the RCS of a truncated right circular cone if the radius a is replaced by the mean radius of the cone and ℓ is replaced by the length of the slanted surface.

Although the theory of physical optics offers a significant improvement over geometric optics for flat and singly curved surfaces, it suffers other drawbacks. Even though we obtain the proper result for most of the illuminated surface, the physical optics integral yields false contributions from the shadow boundaries, as already noted. Moreover, physical optics shows no dependence on the polarization of the incident wave and yields different results when the receiver and the transmitter are interchanged. These effects contradict observed behavior. Finally, it errs by wider margins as the direction of observation moves farther away from the specular direction. Keller's *geometrical theory of diffraction* (GTD) offers an improvement in both the polarization dependence and the predicted values in the wide-angle regions.^{33,34}

Geometric Theory of Diffraction. GTD is a ray-tracing method that assigns an amplitude and phase to fields diffracted at smooth shadow boundaries and at surface discontinuities. Because the latter are much more significant in backscattering computations than the former, we focus here on edge diffraction. The theory assumes that a ray striking an edge excites a cone of diffracted rays, as in Figure 14.19. The half angle of this *diffraction cone* is equal to the angle between the incident ray and the edge. Unless the point of observation lies on the diffraction cone, no value is assigned the diffracted field. The scattering direction in backscattering problems is the reverse of the direction of incidence, whence the diffraction cone becomes a disk, and the scattering edge element is perpendicular to the line of sight.

The amplitude of the diffracted field is given by the product of a *diffraction coefficient* and a *divergence factor*, and the phase depends on the phase of the edge excitation and on the distance between the observation point and the diffracting edge element. Two cases are recognized, depending on whether the incident field is polarized parallel or perpendicular to the edge.

The diffracted field is given by the formula:

$$E_d = \frac{\Gamma e^{iks} e^{i\pi/4}}{\sqrt{2\pi ks} \sin \beta} (X \mp Y) \quad (14.17)$$

where Γ is a divergence factor, X and Y are diffraction coefficients, β is the angle between the incident ray and the edge, and s is the distance to the observation point from the point of diffraction. The difference of the two diffraction coefficients is

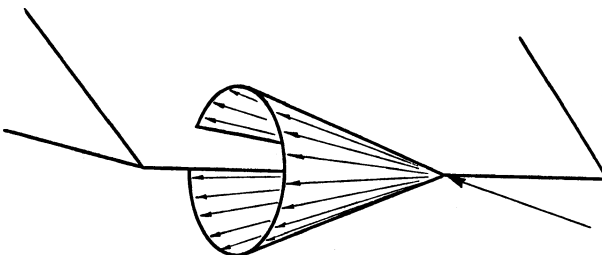


FIGURE 14.19 The Keller cone of diffracted rays

used when the incident electric field is parallel to the edge (*TM polarization*) and the sum when the incident magnetic field is parallel to the edge (*TE polarization*).

The divergence factor accounts for the decay in amplitude as the rays spread away from the edge element and includes the effects of the radius of the edge if it is curved, as at the end of a truncated cylinder, and the radius of curvature of the incident phase front.³⁵ The divergence factor for a two-dimensional edge (of infinite length) illuminated by a plane wave is $\Gamma = 1/s$. The diffraction coefficients are

$$X = \frac{\sin(\pi/n)/n}{\cos(\pi/n) - \cos[(\phi_i - \phi_s)/n]} \quad (14.18)$$

$$Y = \frac{\sin(\pi/n)/n}{\cos(\pi/n) - \cos[(\phi_i + \phi_s)/n]} \quad (14.19)$$

where ϕ_i and ϕ_s are the angles of the planes of incidence and scattering, as measured from one face of the wedge (say, the illuminated one), and n is the exterior wedge angle normalized with respect to π . When these expressions are evaluated for the case of a flat metal edge viewed edge-on with the incident polarization in the plane of the plate, they yield the edge-on formula $\sigma = L^2/\pi$ listed in Table 14.1.

Keller's diffraction coefficients are based on an approximation of the exact solution for an infinite (two-dimensional) metal wedge as applied to a three-dimensional problem.³⁶ Although this adaptation of a two-dimensional solution to the three-dimensional world is reasonably effective most of the time, the diffraction coefficients inconveniently blow up just when needed most. A cursory examination of Eqs. 14.18 and 14.19 will show why.

The denominators of both expressions contain the difference of two cosine terms that become equal in two different cases. When the scattering direction ϕ_s is aligned along the shadow boundary where $\phi_i - \phi_s = \pi$, the diffraction coefficient X in Eq. 14.18 becomes singular, a meaningless result. When the scattering direction ϕ_s is aligned along the specular direction where the local angle of reflection is equal to the local angle of incidence, then $\phi_i + \phi_s = \pi$. In this case, it is the diffraction coefficient Y in Eq. 14.19 that becomes singular, a similarly meaningless result. Note that these two singularities do not depend on body geometry, but only on the relative dispositions of the incidence and scattering directions.

Physical Theory of Diffraction. The singularities in GTD are overcome in the *physical theory of diffraction* (PTD) formulated by P. Ia. Ufimtsev.^{37,38} (Although these publications may be difficult to find, we cite them here for completeness. *Note from the editor:* The reader interested in this subject might also see the Ufimtsev paper "Comments on Diffraction Principles and Limitations of RCS Reduction Techniques," *Proc. IEEE*, vol. 84, pp. 1830–1851, December 1996.) Like Keller, Ufimtsev relied on the approximate (wide-angle) solution of the two-dimensional wedge problem, but he distinguished between "uniform" and "nonuniform" induced surface currents. The uniform currents were none other than the surface currents of physical optics, whereas the nonuniform currents were taken to be undefined filamentary currents along the edge itself. Ufimtsev never attempted to work out his filamentary *fringe* currents, but instead traced their effect directly to the far scattered field.

Recognizing that the far-field PO contribution to the far field was the part of the GTD prescription giving rise to singularities in the X and Y of Eqs. 14.18 and 14.19, Ufimtsev devised a modified set of diffraction coefficients by simply subtracting away

the offensive PO diffraction coefficients from the time-honored wide-angle wedge solution. This generated a new set of diffraction coefficients that retained only the edge terms, therefore excluding any surface terms. Ufimtsev's PTD coefficients were well behaved in almost all directions in space, but suffered one disadvantage: in order to calculate the RCS of an arbitrary edged body, one had to sum all the PTD edge contributions, *plus* all the PO and GO surface contributions. However, the procedure is viable and has been well documented.⁴⁰

Incremental Length Diffraction Coefficient. GTD and PTD are both based on the exact solution of the two-dimensional wedge problem, for which the directions of incidence and scattering are perpendicular to the edge. When extended to the case of oblique incidence, the direction of observation must lie along a generator of the Keller cone depicted in Figure 14.19. If the edge is straight and of finite length, as in the three-dimensional world, Eq. 16 of Knott¹ provides an approximation of the RCS. If the edge is curved, it may be regarded as a collection of infinitesimally short segments butted together, and the scattered fields may be computed via an integration of incremental fields diffracted by each element of the edge. This is the concept introduced by Mitzner,⁴¹ and the summation of the fields diffracted by the edge elements implies an integral around the edge contour.

Mitzner, however, sought the fields scattered in arbitrary directions, not just those along the local Keller cones, and for this purpose he developed his *incremental length diffraction coefficient* (ILDC). Extending the example provided by Ufimtsev, he devised a set of diffraction coefficients for arbitrary directions of incidence and scattering. Not unexpectedly, those coefficients are more complicated than the X_s and Y_s appearing in Eqs. 14.18 and 14.19.

Mitzner expressed his result as the diffracted electric-field components parallel and perpendicular to the plane of scattering in terms of the components of the incident electric field parallel and perpendicular to the plane of incidence. As such, the diffraction coefficients may be expressed as three separate pairs representing parallel-parallel, perpendicular-perpendicular, and parallel-perpendicular (or perpendicular-parallel) combinations. One member of each pair is due to the total surface current on the diffracting edge (including the assumed filamentary edge currents), and the other is due to the uniform physical optics currents. Mitzner subtracted one member of each pair from the other, thereby retaining the contributions from the filamentary edge currents alone.

The results have the identical form of Ufimtsev's expressions, in which the PO coefficients are subtracted from the non-PO coefficients. Thus, Mitzner's expression for the scattered field contains only the contributions from the filamentary edge currents. In applying his theory to scattering objects, therefore, the contributions of nonfilamentary-induced surface currents must be accounted for separately, just as in Ufimtsev's PTD. When the directions of incidence and scattering become perpendicular to an edge, the perpendicular-parallel terms disappear and Mitzner's diffraction coefficients then reduce identically to Ufimtsev's.

Method of Equivalent Currents. Undertaking what he called a more rigorous evaluation of the fields induced on a wedge, Michaeli duplicated Mitzner's result for the total surface currents, confirming Mitzner's prior development, but he did not explicitly remove the PO surface-current contributions.^{42,43} Thus, like Keller's X and Y , Michaeli's diffraction coefficients become singular in the transition regions along

the reflection and shadow boundary directions. Michaeli later investigated the removal of the singularities, the cleverest of which was the use of a skewed coordinate system along the wedge surfaces.^{44,45}

While these methods of evaluating the fields scattered by edge elements may be applicable to smooth unbounded edges, they do not account for the discontinuities at corners where the edges turn abruptly in other directions. An attack on the corner problem has been suggested by Sikta et al.⁴⁶

14.4 RCS MEASUREMENT TECHNIQUES

RCS measurements may be required for any of several reasons, ranging from scientific inquiry to verification of compliance with product specifications. There are no formal standards governing instrumentation and measurement methods, but informal standards of good measurement practice have been recognized for decades. Depending on the size of the test object, the frequencies to be used, and other test requirements, measurements may be made in indoor test facilities or on outdoor ranges. Because one is seldom interested in the RCS of an object for only one aspect angle, all static test ranges use turntables or rotators to vary the target aspect angle. Although the purpose of testing often governs how the measurements will be made, Mack and Dybdal provide good overall guides for routine RCS testing.^{47,48}

General Requirements. The most important requirement for RCS measurements is that the test object be illuminated by a radar wave of acceptably uniform amplitude and phase. Good practice dictates that the amplitude of the incident wave deviate by no more than 0.5 dB over the transverse and longitudinal extent of the target and that the phase deviation be less than 22.5°. It is standard practice at some test ranges to physically probe the incident field at the onset of a test program to verify the amplitude uniformity of the incident wave.

The phase requirement is the basis of the far-field range criterion:

$$R > 2D^2/\lambda \quad (14.20)$$

where R is the distance between the instrumentation radar and the test object and D is the maximum target dimension transverse to the line of sight. All other error sources being fixed, compliance with the far-field requirement is generally felt to yield data with an accuracy of 1 dB or better.⁴⁹ Figure 14.20 illustrates the far-field requirement for a variety of frequencies and target sizes.

Errors attributable to radar instrumentation should be held to 0.5 dB or less, which requires careful design and selection of components. The drift in system sensitivity should not exceed this value for the time it takes to record a single RCS pattern, which sometimes may approach an hour. The dynamic range of the system should be at least 40 dB, with 60 dB preferred. Linearity over this range should be 0.5 dB or better, and if not, steps should be taken to correct measured data via calibration of the receiver transfer function (gain characteristics).

RCS measurements should be calibrated by the *substitution method*, in which an object of known scattering characteristics is substituted for the target under test. Given the known (measured or calibrated) receiver gain characteristics, this establishes the constant by which a receiver output indication may be converted to an absolute RCS value.

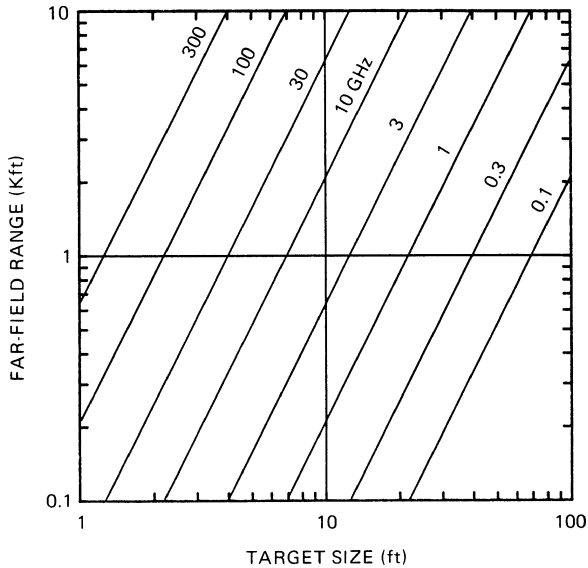


FIGURE 14.20 The far-field distance (Reprinted with permission of SciTech Publishing, Inc.⁵⁰)

Common calibration targets include metal spheres, right circular cylinders, flat plates, and corner reflectors. The radar cross sections of these objects may be calculated by using the expressions given in Section 14.3.

Because residual background reflections contaminate the desired target echo signal, they should be minimized by careful range design and operation. Interior walls in indoor test chambers must be covered with high-quality radar-absorbing material, and the surface of the ground on outdoor ranges should be smooth and free of vegetation. Target support structures should be designed specifically for low echo characteristics.

The effects of undesired background signals are illustrated in Figure 14.21. Because the relative phase between the background signal and the target signal is unknown, two curves are shown; they correspond to perfect in-phase and out-of-phase conditions. If the background signal is equal to the target signal (ratio of 0 dB) and the two are in phase, the total received power is four times the power due to either one. This is the value shown at the upper left of the chart (6 dB). If the two are out of phase, they cancel each other, and there is no signal at all (off the lower left of

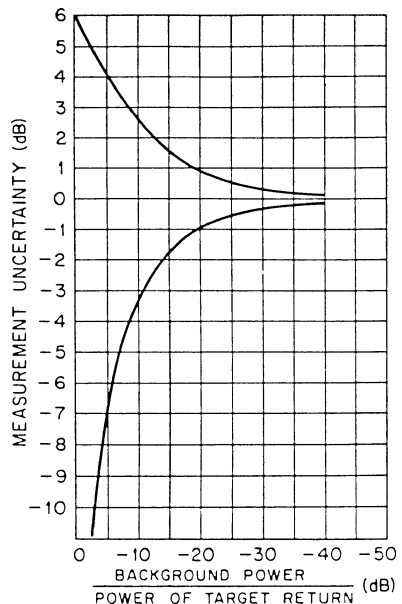


FIGURE 14.21 Measurement error as a function of the relative background power level

the chart). The chart shows that if the error due to background signals is to be 1 dB or less, the background must be at least 20 dB below the signal being measured.

Three different kinds of support structures have been demonstrated to be useful in RCS measurements. They are the low-density plastic foam column, the string suspension harness, and the slender metal pylon. The echo from a plastic foam column arises from two mechanisms. One is a coherent surface reflection, and the other is a noncoherent volume contribution from the thousands of internal cells comprising the foam material.^{51,52} The column should be designed so that its surfaces are never closer than 5° to 10° to the line of sight to the radar (depending on frequency), thereby minimizing the effect of the surface reflection. The noncoherent volume return is irreducible, however, and is not influenced by the orientation of the column. The volume return of suitable foam column support materials is of the order of $1.6 \times 10^{-6} \text{ m}^2$ per ft^3 of exposed column at 10 GHz.⁵³

String suspension methods are best implemented indoors, where an overhead support point is normally available, although one documented design was seriously considered for outdoor use.⁵⁴ One of three configurations may be selected, all requiring a custom-made sling or harness to support the target. The first uses a single overhead support point and guy lines to a floor-mounted turntable to rotate the target. The second configuration suspends the target from an overhead turntable, reducing the guy lines and string loads at the expense of a more costly installation. The third configuration is the most costly, using a pair of turntables slaved together, one in the ceiling and one on the floor.

The echo signal from a string depends on the length and diameter of the string, its tilt angle with respect to the incident wave, and its dielectric constant. No matter what the tilt of the string, it will be presented normal to the line of sight twice in a complete rotation of the target and may cause a spike in the RCS pattern that could be erroneously attributed to the target unless otherwise accounted for. The RCS of a string rises with the fourth power of its diameter in the Rayleigh region (see Figure 14.4), and for a given tensile strength, the diameter rises only as the square root of the load to be supported. Thus, because the echo signal increases with the square of the load-carrying capacity, string suspension techniques are best suited for measurements of light objects at low frequencies.

The metal target support pylon was first suggested in 1964,⁵⁴ but a practical implementation of the concept did not appear until 1976. The configuration of the pylon is shown in Figure 14.22, and it owes its electromagnetic performance to the sharpness of its leading edge and its tilt toward the radar (to the left in the diagram). Pylons as tall as 95 ft have been built, and it is customary to treat them with radar-absorbing material to suppress the echoes from the leading and trailing edges.

The obvious advantage of the metal pylon is its superior weight-carrying capability compared with that of strings and plastic foam columns. However, because the top of the pylon is small, the rotation mechanism needed to vary the aspect angle of the target must be embedded in the target itself. This usually destroys the operational value of the target. Most of the rotators for these pylons are dual-axis, azimuth-over-elevation designs. When measurements are made with the azimuth rotation angle tilted back (away from the radar), parts of the target may sweep through the shadow cast by the top of the pylon, possibly degrading the measurements. One way to avoid this is to invert the target and tilt the rotation axis toward the radar instead of away from it. This requires the installation of the rotator in the top of the target as well as in the bottom. The unused internal cavities created for such installations must be concealed by covers or shields.

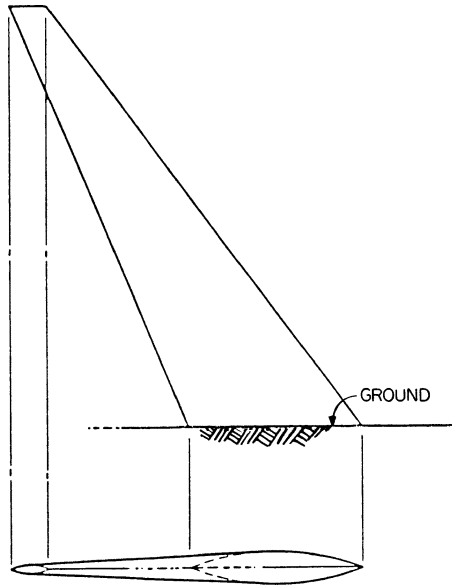


FIGURE 14.22 The metal support pylon. The design is for an incident wave arriving from the left. (*Reprinted with permission of SciTech Publishing, Inc.*⁵⁵)

It is often necessary to measure scale models, which requires the application of scaling laws. Because nonconducting materials must be scaled differently than good conductors, it is not possible to satisfy all the scaling requirements for arbitrary targets composed of conducting and nonconducting materials. Most targets requiring scale-model testing, however, are dominantly metallic, for which the perfectly conducting scaling law is generally regarded as adequate.

When normalized with respect to the square of the wavelength, the RCS patterns of two perfectly conducting objects of identical shape but different size will be identical if the objects are the same number of wavelengths in size. If a model is one-tenth of full scale, for example, it should be measured at one-tenth of the full-scale wavelength (ten times the full-scale frequency). The RCS of the full-scale target may be obtained from the scale-model measurements by multiplying the scale-model RCS by the square of the ratio of the two frequencies. In this example, that factor is 10^2 , or 20 dB.

Outdoor Test Ranges. Outdoor test ranges are required when test targets are too large to be measured indoors. The far-field criterion often requires that the range to the target be several thousand feet (see Figure 14.20). Because the typical target height above the ground is a few dozen feet at best, the elevation angle to the target as seen from the radar is 1° at most and often less. At such low grazing angles, the ground is strongly illuminated by the antennas, and unless the ground bounce can be suppressed, the target will be illuminated by a multipath field. In the design of an outdoor test range, therefore, a decision must be made whether to exploit the ground bounce or to attempt to defeat it. It is generally easier to exploit it than to eliminate it.

Test ranges designed to exploit the multipath effect may be asphalted to improve the ground reflection, although many ranges are operated over natural soil. Paving the range ensures uniformity in the characteristics of the ground plane from day to day and extends its operational usefulness to higher frequencies than might otherwise be possible. A conducting screen embedded in the asphalt may improve the reflection. Paving also reduces maintenance of the ground plane, such as might be required by periodically removing vegetation and smoothing out windblown ridges in unstable soil.

The angle of incidence and the dielectric properties of asphalt and natural soil are such that the phase of the voltage reflection coefficient is within a few degrees of 180° . This being the case, one can usually choose a combination of target and antenna heights such that the wave reflected by the ground arrives at the target in phase with the wave propagated directly from the antennas. The result is the following rule for selecting the antenna and target heights:

$$h_a h_t = \lambda R / 4 \quad (14.21)$$

where h_a and h_t are the antenna and targets heights, respectively, and R is the range to the target.

Because most test ranges have turntables or target pylons installed at a few fixed locations relative to a permanent radar complex, the range R is usually restricted to a few preset values. The target is installed at a height h_t high enough to minimize spurious interactions with the ground, yet low enough to minimize the size and complexity of the target support structure. Therefore, it is the antenna height h_a that is most readily controlled and adjusted to optimize the location of the first lobe in the vertical multipath interference pattern. This is easily accomplished by mounting the radar antennas on carriages that can be raised or lowered along rails installed on the side of a building or a tower.

The ideal ground plane offers a theoretical sensitivity enhancement of 12 dB over identical measurements made in free space. The actual enhancement is usually less than this, primarily because of the directivity of the antennas and imperfections in the ground plane. Antenna directivity precludes the target ever being squarely aligned on the boresights of both the real antenna and its image in the ground plane at the same time, and the reflection coefficient of typical ground planes varies from 95% to as low as 50% or less. For all except very high and very low frequencies (millimeter wavelengths and VHF), typical sensitivities are of the order of 7 to 10 dB above free space instead of the ideal 12 dB.

When the range to the target is relatively short and tests must be performed over a wide range of frequencies, it is sometimes advantageous to attempt to defeat the ground-plane effect. One option is to install a berm shaped like an inverted V running between the radar and the target. The purpose of the berm's slanted top is to deflect the ground-reflected wave out of the target zone. Another option is to install a series of low *radar fences* across the range. The design objective is to block ground-reflected rays from reaching the target from the radar, and vice versa, by shielding the specular zone on the ground from both. The near sides of the fences should be slanted to deflect energy upward (out of the target test zone) and may be covered with absorbing material. It is difficult, however, to prevent diffraction of radar energy from the top of the fences from reaching the target or to prevent target-diffracted signals from reaching the radar receiver via the same kind of mechanism.

Because of the large distances from the radar to the target on outdoor ranges, instrumentation radars at one time developed peak signal powers ranging from 1 to 100 kW.

The high-power instrumentation of yesteryear has been largely replaced on static test ranges with coherent stepped-frequency radars that are far more versatile, but high-power systems remain useful for dynamic testing of targets flying or sailing past them on dynamic test ranges. Stepped- and swept-frequency instrumentation systems on static ranges can collect RCS patterns at hundreds of frequencies for a single rotation of the test target. The signal-to-noise ratio can be improved when necessary by means of multisweep or multistep signal integration schemes. The price paid for much of this versatility is the requirement for more active test time per target rotation, thereby increasing measurement costs.

Indoor Test Ranges. Indoor test ranges offer protection from weather and therefore more productive testing, but unless a very large facility is available, maximum target sizes are limited to one or two dozen feet. Because of their proximity, the walls, floor, and ceiling must be covered with high-quality absorbing material. The lower the intended frequency of operation, the more expensive the absorber becomes. Absorber reflectivity ratings of -50 dB are common among the materials used. This performance is usually achievable only with the pyramidal design.⁵⁶

Early indoor chambers were rectangular in shape, and despite the installation of good absorbent materials on the walls, RCS measurements could be contaminated by wall reflections. The most sensitive part of the anechoic chamber is the rear wall, which receives 95 to 99 percent of the power radiated by the radar; hence, the best absorber should be reserved for the rear wall.⁵⁷ The floor, ceiling, and sidewalls also contribute errors, via a quadruplet of reflections not unlike those due to the ground plane of outdoor ranges. A remedy is the tapered anechoic chamber, which eliminates most of the sidewall reflections purely by tilting portions of the walls, floor, and ceiling away from the chamber centerline.^{58,59,60}

Even targets of modest size cannot be measured at the far-field distance in indoor facilities because most chambers are not much more than 200 ft or so in length. It is possible, however, to provide the necessary uniformity of illumination by *collimating* the radiated beam. This can be done by inserting a lens between the radar and the target^{61,62} or by reflecting the radar beam off a collimating reflector. This latter concept is known as the *compact range* because a beam of parallel rays can be generated in a much shorter distance than would be possible without the collimating device.

The reflector offers a different way to collimate a beam. In contrast to the lens, which is placed between the radar and the test object, the radar and the test object remain on the same side of the reflector, as shown in Figure 14.23. The reflector is typically an offset paraboloid, meaning the paraboloidal surface does not include the vertex of the generating parabola. This permits the feed that excites the reflector to be placed out of the beam reflected toward the target. If the test object is held within one or two focal lengths of the reflector and if the reflector is excited by a suitably designed feed, the reflected wave is sensibly planar.⁶¹

However, unless the edges of the reflector are carefully designed, the incident field in the target zone will be contaminated by undesired fields diffracted from the edges of the reflector. The diffraction causes ripples in both the amplitude and the phase of the field distribution in the target zone. In some cases, the effect is small enough to be ignored, but in high-quality installations, the ripple may be objectionably large. Rolled-edge configurations, such as the one on the upper edge of the main reflector in Figure 14.24, can be designed to minimize edge diffraction.^{62,63} However, the price paid for this improvement in performance is a much larger and more complicated reflector structure.

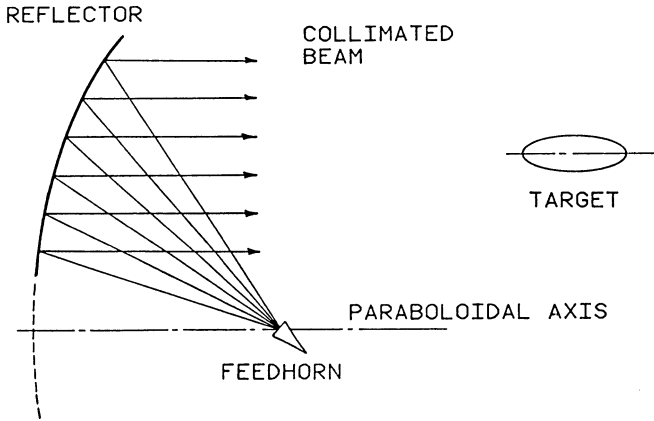


FIGURE 14.23 A compact range using an offset paraboloidal reflector

The single-reflector design shown in Figure 14.23 worked tolerably well for small test targets, but it soon became apparent that the reflector had to be considerably larger for many targets of vital military interest. This could be accomplished by doubling or tripling the size of the reflector, but that brought on a round of other problems, mainly the increased focal length of the reflector. While the focal distance could be shortened to comfortably fit axial space limitations (along the boresight of the reflector), it was then harder to control the field amplitude taper across the reflector due to the proximity of the feedhorn. The solution was to add a smaller subreflector in a subterranean gallery built especially for it, as suggested in Figure 14.24.^{63,64}

The subreflector had the effect of greatly increasing the focal length of the main reflector, making it easier to optimize its illumination. This particular configuration is known as a *Gregorian system*, characterized by a focus between the two reflectors

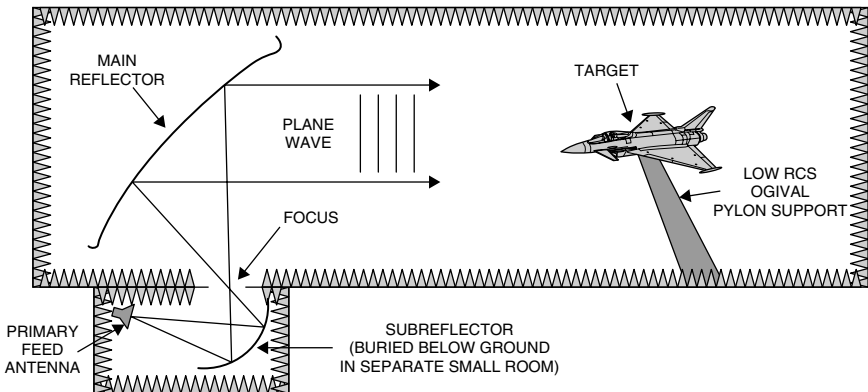


FIGURE 14.24 Generic dual-reflector compact range configuration²⁰

where most of the rays between the two reflectors converge. In a second configuration known as the *Cassegrain*, the focus is a virtual one lying behind the subreflector. The Gregorian configuration permits the construction of a smaller aperture between the main chamber and the subreflector gallery than does the Cassegrain configuration.⁶⁵

Large compact ranges such as the one shown in Figure 14.24 are very costly and can be afforded by only the largest of companies (or the government), thus range time is premium. Some companies keep their compact ranges busy 24 hours per day.

Targets measured indoors are placed much closer to the radar than those measured outdoors, and useful measurements may be made by using much less radiated power. Early indoor instrumentation radars relied on simple CW sources, and undesired chamber reflections were suppressed by a cancellation process. The procedure is to prepare the chamber for a measurement in every respect except for the installation of the target on its support fixture. A small sample of the transmitted signal is passed through a variable attenuator and a variable phase shifter and combined with the received signal. The amplitude and phase of the signal sample are then adjusted so as to cancel the signal received in the absence of the target.

The availability of low-cost, phase-locked, frequency-synthesized sources now makes it attractive to collect wideband RCS data, which contain far more target-scattering information than CW measurements made at single frequencies. When coherent RCS scattering data are suitably processed, it is possible to generate *ISAR imagery*, or two-dimensional maps of the echo sources of test objects.⁶⁶

Figure 14.25 is an example of such an image. In this case, the processing required to generate this image is a double Fourier transformation, one from the frequency domain to the time domain and the other from the angle domain to the cross-range domain. The frequency-time domain processing may be performed virtually in real time (a second or two for processing and display on a video screen), but the conversion

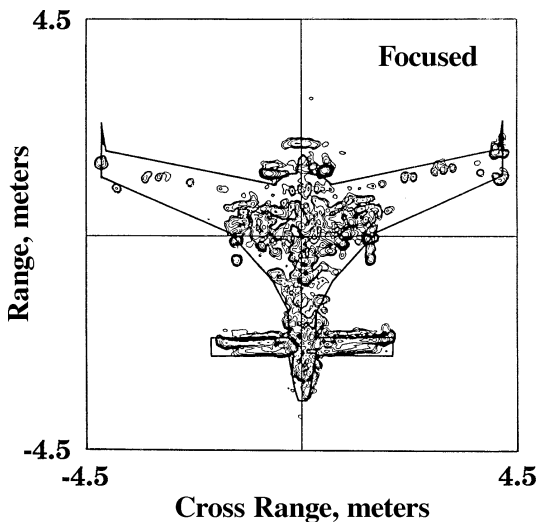


FIGURE 14.25 Radar image of a small drone aircraft. Planform outline has been added for clarity. (Courtesy D. L. Mensa, U.S. Navy Pacific Missile Test Center.)

from the angle domain to the cross-range domain must be performed offline in this example. The fast Fourier transform (FFT) is invariably exploited to expedite the processing.

The image data presented in Figure 14.25 were collected for a stepped-frequency signal with a bandwidth of 2.1 GHz centered at 3.4 GHz. The aspect angle was varied over a sector 35° wide centered on the nose-on aspect. The charted image contours are 5 dB apart and the total amplitude variation is 30 dB.

The resolution of the processed image in the time (range) domain is inversely proportional to the bandwidth of the emitted waveform. The resolution in the cross-range domain is inversely proportional to the aspect angle window over which the data are collected. Thus, the operating characteristics of the instrumentation system and the azimuthal data sampling rate must be decided before the data are collected. Because the cross-range coordinate of the resulting image is perpendicular to the axis of rotation of the target, it may be necessary to multiply that coordinate by a scale factor that effectively registers the generated image with, say, a plan view of the target.

The resulting data may be presented in the form of a contour map, as in Figure 14.25, or in a color-coded or grayscale pixel format. Here, the target outline has been superposed on the image data for diagnostic analysis, and the particular attitude shown is for nose-on incidence. Similar images can be generated for other angles of incidence, provided the target is rotated through a sector wide enough to yield the desired cross-range resolution and sampled at a sufficient number of angles over that sector. In practice, the target is rotated continuously while the swept- or stepped-frequency data are collected. A rule of thumb is that the angular speed be slow enough that the phase of the return at the end of a frequency sweep due to target motion not be more than 22.5° from what it would have been had the target not moved.

Note that the nose section of the drone is speckled with heavy concentrations of scattering centers, possibly due to contributions from internal structural features. The rear edges of the forward canards seem to be stronger scatterers than the leading edges. At the nose-on aspect angle for which the image data were collected, the leading edges of the wings are virtually invisible. However, note a few echo sources along a line parallel to, and slightly forward of, the wing trailing edges. If the target rotation had been centered on an aspect angle perpendicular to one of the wings, the leading edge of that one wing would have “lit up.”

In the region of the main wing roots, we see heavy concentrations of echo sources. Some of them lie forward of any wing surface. Although we may conceive of apparent sources being strung out behind any physical scattering obstacle due to time delays of multiple reflections, it is hard to reconcile them being strung out *in front* of the body. We do see several clusters of apparent scattering centers positioned aft of the tail of the aircraft, but lacking any detailed description of the test object, we cannot interpret their meaning.

These “ghost” scatterers owe their existence to the way in which the data-processing system sorts the range and cross-range locations of scatterers. Down-range locations are sorted according to their processed time delays and cross-range locations according to their time-delay rates, whether due to real scatterers or to interactions between scatterers. Even though the contributions of some scattering centers may involve propagation in directions other than along the line of sight from the radar, the system has no way of discerning that fact. Therefore, despite the powerful diagnostic value of images like these, one must always be aware that multiple interactions between target elements can create scattering sources that are not where they appear to be.

14.5 RADAR ECHO SUPPRESSION

The probability of being detected by hostile radars can be reduced by decreasing the target's radar cross section. The major methods to reduce the RCS are by shaping of the target and the use of absorbers. By shaping, we mean the intentional selection of target surfaces and features so as to minimize the amount of energy scattered back to the radar. Shaping includes specific design configurations, such as the placement of engine intakes, which can have large radar echoes, where they may be shielded from the incident wave by other parts of the target. The purpose of radar-absorbing materials (RAM) is to absorb the incident radar energy so as to minimize the energy scattered back to the radar. Both methods have advantages and disadvantages.

Radar Absorbers. The purpose of the radar absorber is to attenuate incident energy and thereby reduce the energy scattered or reflected back to the radar. Most absorbers are designed to reduce specular reflections from metallic surfaces, but stealth technology has spawned the development of nonspecular absorbers intended primarily to suppress echoes due to surface traveling waves.

The simplest specular absorber is the *Salisbury screen*, which is a thin resistive sheet mounted a quarter wavelength above the metal surface to be hidden from a radar.⁶⁷ The design works best for incidence normal to the sheet, and if it can be manufactured with a resistivity of 377 ohms per square (the impedance of free space) all the power in the incident wave is transferred to the sheet and none is reflected. However, the single-sheet Salisbury screen suffers several limitations. Its thin sheets and low-loss spacers are fragile, its 20-dB bandwidth is barely 25%, and its performance deteriorates progressively as the angle of incidence moves away from normal incidence.

It is difficult to overcome the fragility problem with robust materials, but the bandwidth can be improved by cascading several sheets, as shown in Figure 14.26. This creates what is known as a *Jaumann absorber*. The bandwidth rises with the number of layers and can attain a respectable 140% for a four-sheet design, as suggested in Figure 14.27. The price paid for this bandwidth expansion is a much thicker, bulkier material that tends to be impractical for tactical military targets.

Like the Salisbury screen, the *Dällenbach layer* is also a simple absorber. The material is uniform throughout its volume and is a mixture of compounds designed to have a specified index of refraction. That design may include materials with magnetic losses as well as carbon particles responsible for electric losses. Therefore, the electric and magnetic susceptances (relative permittivity and relative permeability) have imaginary components, resulting in an index of refraction with an imaginary component.

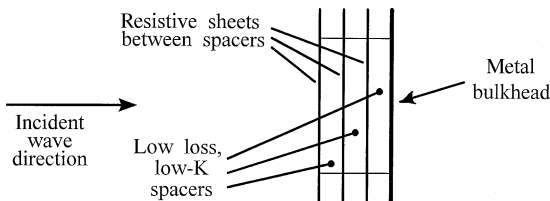


FIGURE 14.26 The Jaumann absorber is a cascaded collection of thin resistive sheets stacked in front of a metal bulkhead, spaced $\lambda/4$ apart, where K = spacer dielectric constant. The classic Salisbury screen is the degenerative case of a single sheet.

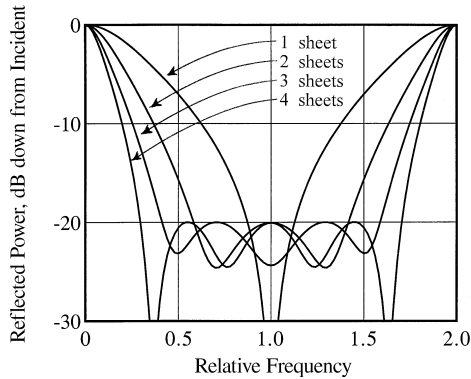


FIGURE 14.27 Performance of Jaumann absorbers with as many as four sheets. All four of these traces were optimized for maximum bandwidth at the -20 dB level. The sheet resistivities must increase from a low value at the inner sheet to a high value at the outer sheet.

The resulting imaginary part of the propagation constant attenuates waves traveling through the material.

Most of the commercial versions of Dallenbach absorbers are flexible and can be applied to modestly curved surfaces. The dielectric absorbers are typically made of a rubbery foam, sometimes urethane, impregnated with carbon particles. Impregnation may be performed by dipping a compressed slab of material in a graphite suspension bath, then wringing it out and drying it. Magnetic Dallenbach layers can be rolled from a mixture of natural or synthetic rubber loaded with carbonyl iron or ferrite powders. The lower the powder content, the more flexible the sheet but the less effective its electromagnetic performance. Dielectric and magnetic Dallenbach layers typically range from about 1 mm to 1 cm in thickness. The magnetic versions are as heavy 320 lb/ft³, making them impractical for most tactical applications.

The front face and the metal backing of the Dallenbach layer are its only sources of reflection. The use of physically realizable materials makes it impossible to force either reflection to zero. The design objective, therefore, is to choose the electrical properties of the layer so that the front-face and metal-back reflections tend to cancel each other. If the material properties are dominated by electric effects, the optimum layer thickness is close to $\lambda/4$, as measured in the material. If they are dominantly magnetic, the layer can be much thinner.

As with the simple Salisbury screen, Dallenbach layers can be cascaded in attempts to expand bandwidth, producing what is known as *graded absorbers*. For optimum performance, the intrinsic impedance of each layer typically gets smaller the closer the layer is to the metal bulkhead or backing layer. Five or more layers have been used in the commercial production of graded dielectric absorbers, but commercial-graded magnetic absorbers appear to have been limited to three layers. It is important in the design process to account for the actual thickness and electrical properties of the adhesive films used to bond the layers to each other. These materials are too flimsy or too heavy for most military applications.

The pyramidal absorber used to suppress wall reflections in indoor chambers represents a particularly effective method of varying the effective impedance “seen”

by an incident wave. The absorber is made of flexible, carbon-impregnated plastic foam cut in the form of pyramids. It exhibits optimum performance when the pyramids are pointed toward the direction of the incident wave, and the pyramids should be of the order of 3 to 6 wavelengths deep. Fire-retardant paint is usually applied to pyramidal absorbers to satisfy safety requirements, but at high frequencies, the paint tends to degrade the performance of the material. Nevertheless, pyramidal absorbers of sufficient depth consistently turn in performances better than (less than) -50 dB. Because these absorbers do not rely on the cancellation of a front-face reflection by a rear-face reflection, they exhibit great bandwidth. In general, a pyramidal absorber with sharp tips and uniform bulk loss characteristics can have a bandwidth that exceeds 100:1.⁶⁰

Nonspecular absorbers need not have the great thickness characterized by specular absorbers. Intended primarily for suppression of surface traveling-wave echoes, nonspecular materials have the opportunity to reduce the buildup of surface currents over several wavelengths *along the surface*. They are able to register quite respectable performances, therefore, simply because a thin layer attached to a metallic surface need not be very heavy. In this respect, the surface traveling-wave contribution due to long, smooth surfaces is one of the easiest to suppress. Even so, the thickness and geometric distribution of surface-wave absorbers should be varied for optimum performance.

By this point, it should be apparent that the application of radar absorbing materials to vulnerable targets is not a very effective way to enhance their survivability. These materials are heavy, demand undue surface care and maintenance, suffer limited bandwidth, and not least, are costly. A far more viable option, target shaping, is usually available if one is willing to consider it at the onset of system development.

Shaping. Shaping is the result of judiciously orienting target surfaces and edges in a way that minimizes their contributions to the total radar echo. This often means selecting airframe shapes and naval hull profiles that initially outrage airframe designers and naval architects. But there is no point in considering shape control unless a specific threat direction can be identified in azimuth or elevation or both. If all directions are equally likely, then the advantage of choosing favorable surface orientations for one threat direction is canceled by an accompanying enhancement in another. In many situations, however, the general direction of the threat can be forecast.

Figure 14.28 illustrates the RCS reduction available through shaping. The plotted curves are based on theory and measurements and show how the nose-on (axial) RCS varies with the electrical size of each of the six rotationally symmetrical metallic bodies shown in Figure 14.29. The diameters and projected areas of the objects are identical, and their volumes differ at most by a factor of 2. Except for the sphere, whose geometric-optics RCS is shown by the uppermost trace, all the objects have the same nose angle (40°), and of the six shapes, the ogive exhibits the lowest RCS. Thus, at least along the axes of these particular bodies, the RCS can be minimized by selecting the appropriate surface profile.

However, the attainment of low echoes over a range of aspect angles is usually accompanied by higher echo levels at other angles. Thus, the selection of an optimum shape should always include an evaluation of the variation of the RCS over a range of aspects wide enough to cover the anticipated threat directions. This implies the capability to measure the RCS patterns of a collection of objects with candidate surface profiles or the capability to predict those patterns, or both.

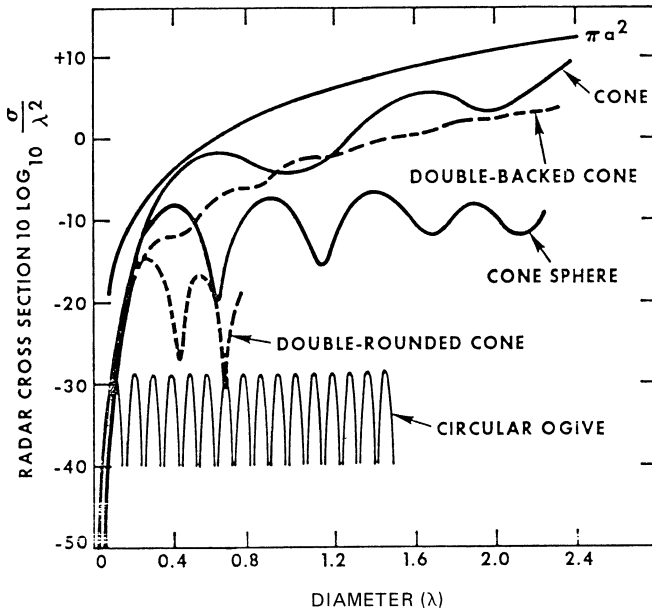


FIGURE 14.28 RCS of a collection of bodies of revolution of similar size and projected area (after W. E. Blore⁶⁸ © IEEE 1964)

Two approaches may be taken in the application of shaping. One is to replace flat surfaces with curved surfaces and thereby eliminate narrow but intense specular lobes. This is not very effective because it increases the general echo levels at nearby aspect angles. The second approach is to extend flat and singly curved surfaces so as to further narrow the specular lobe even if this increases its intensity. The logic of this approach is that the probability of detection is proportional to the average RCS over a range of solid angles of observation, and if the width of the lobe is narrow enough, its contribution to the average RCS may be less than if it were a wider but less intense lobe. The required RCS pattern levels of specific vehicle concepts should be established by means of mission analyses before deciding which shaping criterion is applicable.

Shaping is usually difficult to exploit or expensive to implement for vehicles or objects already in production because the vehicle configuration and profile have been selected and optimized for specific mission objectives. Changes in the configuration after production, therefore, are likely to impair the mission capabilities of the vehicle. If considered an option in the control of RCS, shaping must be included in the conceptual design of the vehicle well before any production decisions are made. Furthermore, shaping is not very effective for bodies that are not electrically large.

Low Radar Cross Section Vehicles. The following are some examples of low cross section vehicles from the early days of low cross-section vehicle design.

The SR-71. The design of low cross-section vehicles probably began when Clarence ("Kelly") Johnson, Lockheed's famous designer, undertook development

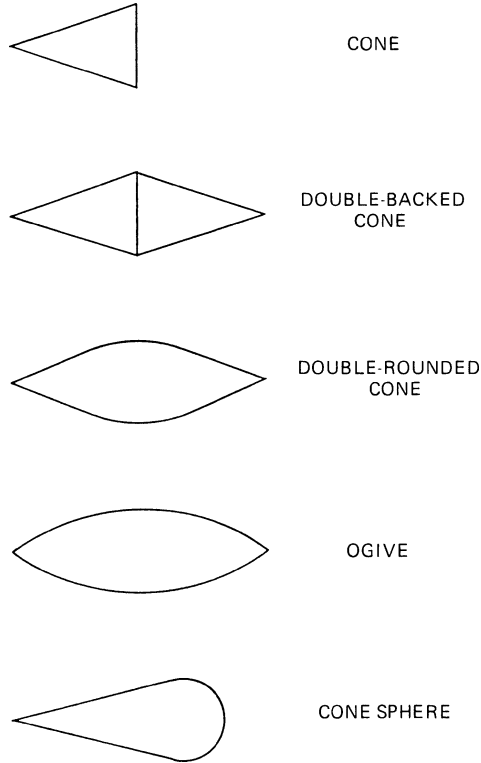


FIGURE 14.29 The objects whose radar cross sections are plotted in Figure 14.28.

of the A-12, an early prototype of the SR-71 Blackbird reconnaissance platform. At Lockheed's fabled Skunk Works, he recognized the importance of bringing the RCS design engineer into the inner-circle design team. The A-12 development contract was awarded in 1959,⁶⁹ and by early 1964 the A-12 was flying missions around the world.

The influence of Johnson's radar signature specialists is evident in Figure 14.30. The most remarkable feature of the SR-71 is the chine that runs from the nose to the root of the delta wing. In the nose-on sector, the radar echo will be dominated by returns from the engine inlets where the chine contribution is no doubt negligible. When seen from the broadside aspects, the chine reduces the specular echo that would have come from the otherwise rounded sides of the forward fuselage. Note that the tail fins are canted inward, thereby deflecting incident radar waves upward (away from the radar) when seen from the side. This design greatly reduces the SR-71's echo in a narrow broadside sector of angles.

The F-117. The largest echo source in the SR-71 nose-on region is probably the engine intakes because they are thrust well forward of the wing leading edges. The intakes of the F-117 Nighthawk, by contrast, are installed above the wing and well aft of the leading edge; they are the little black diamonds seen in the nose-on view of the F-117 shown in Figure 14.31. As such, the intakes are shielded from ground-based






 Dryden Flight Research Center EC96- 43902- 1
 SR-71B photographed from Air Force tanker.
 28Jan1997 NASA photo by Jim Ross
 

FIGURE 14.30 Lockheed's SR-71 Blackbird

radars when the F-117 is in level flight. Even so, the F-117 developers contrived an egg-crate covering for the intakes that, in theory, prevents approaching radar waves from entering the inlet ducts, where they rattle around and eventually come back out again, heading directly back to the radar.⁷⁰

Because the egg-crate grillwork reduced airflow, the intake had to be enlarged to restore normal flow. And the designers later discovered that the grillwork tended to ice up, which they overcame with an electrical heating system. The most remarkable features of the F-117 are its faceted (aerodynamically poor) surface profile and its

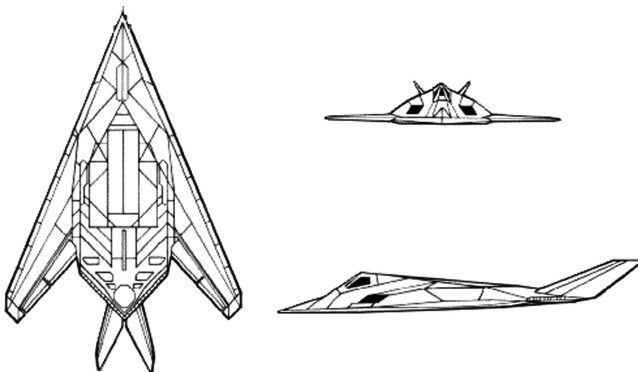


FIGURE 14.31 Lockheed's F-117 Nighthawk fighter

sharply swept tail fins. The tail fins are canted out as well as being swept aft, and the wings are also sharply swept. Although Lockheed managed to produce a supersonic SR-71 airframe using exotic materials, the low RCS demanded of the F-117 required a subsonic airframe. The airframe is covered with thin absorbing material whose edges are serrated to reduce reflections where hatches and covers fit into the fuselage.

B-2 Spirit Bomber. Northrop, the prime contractor for the B-2 Spirit, faced the same problem with engine placement that Lockheed did with the F-117 Nighthawk. The solution was the same: embed the engines' intakes in the top side of the airframe. Possibly because the B-2 had a different mission than the F-117 did, Northrop did not install egg-crate grillwork over the engine intakes. Indeed, Northrop designers devised hinged cowlings that open up at landing and takeoff speeds to increase air-flow into the engines. The cowlings are then retracted at cruising speed for optimum thrust and efficiency.

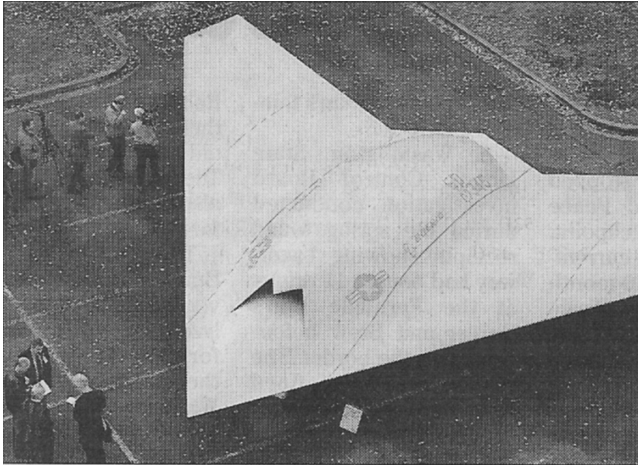
In the interest of lowering the airframe's radar echo, Northrop's design team deliberately built the B-2 without a tailfin. Aside from this, it is interesting that the F-117 and B-2 share some common features. One is the rounded wingtips, which tend to reduce tip-spawned reflections of surface traveling waves that might build up along the wing's leading edges. Another is the use of thin absorber coatings that are serrated around the edges of hatches, covers, and canopies to suppress reflections from edge discontinuities. Yet another is the fact that the B-2, like the F-117, has a subsonic airframe. This suggests that although the chine concept may have worked for the fuselage of the fabled Mach-3 SR-71, it is by no means a viable approach for reducing the echoes from wing leading edges.

Indeed, the designers of the B-2 airframe apparently recognized early in the design work that it would be nearly impossible to reduce the leading edge RCS of their subsonic airframe to acceptable levels. That being the case, they decided to angle all leading and trailing edges at a common sweep angle: 34° . Their philosophy was that if they couldn't suppress the edge returns, the next best option would be to angle them all into four common directions in space. Thus, all trailing edges in the B-2 are parallel to leading edges.

X-45C Unmanned Combat Vehicle. The Boeing Company unveiled a mockup of the "C" version of its unmanned combat vehicle in the mid-2000s, less than a decade after the project was funded by the Defense Advanced Research Projects Administration (DARPA). An Associated Press photo of the aircraft mockup is shown in Figure 14.32. The airframe is 49 ft wide and 39 ft long.

The nose angle of the planform is nearly double that of the F-117, yet barely half that of the B-2, so the planform nose angle seems to be a compromise between the two. Note that the absence of a cockpit improves the stealthiness of the airframe. Indeed, the engine inlet cowling replaces the cockpit, and even the lips of the inlet are broadly serrated to reduce their contribution to the radar echo. The lack of any tailfin and the contour of the trailing edges of the planform reveal strong influences from the B-2 design philosophy.

Low Cross Section Ships. Conventional ships usually have very large structures with many horizontal and vertical reflecting surfaces that meet at right angles, forming corner reflectors with strong echoes. They also can have many individual scatterers that can contribute to a large radar cross section. To achieve low radar cross section, the horizontal/vertical design plan is changed so as to employ tilted surfaces



KEVIN P. CASEY ASSOCIATED PRESS

FIGURE 14.32 Boeing's mockup of its X-45C unmanned combat vehicle
(Courtesy of the Associated Press)

that spoil the corner-reflector effect. Surface tilting also moves the radar angle of incidence well into the far sidelobes of most surfaces on the vessel. Thus vertical bulkheads often are tilted inboard.⁷¹

REFERENCES

1. E. F. Knott, "Radar observables," in *Tactical Missile Aerodynamics: General Topics*, Vol. 141, M. J. Hensch, ed., Washington, DC: American Institute of Aeronautics and Astronautics, 1992, Chap. 4.
2. E. G. Schneider, "Radar," *Proc. IRE*, vol. 34, pp. 528–578, August 1946.
3. S. D. Robertson, "Targets for microwave navigation," *Bell Syst. Tech. J.*, vol. 26, pp. 852–869, 1947.
4. J. A. Stratton, *Electromagnetic Theory*, New York: McGraw-Hill Book Company, 1941, pp. 414–420, 563–567.
5. J. Rheinstein, "Backscatter from spheres: A short-pulse view," *IEEE Trans.*, vol. AP-16, pp. 89–97, January 1968.
6. D. Atlas, L. J. Battan, W. G. Harper, B. M. Herman, M. Kerker, and E. Matijevic, "Back-scatter by dielectric spheres (refractive index ~ 1.6)," *IEEE Trans.*, vol. AP-11, pp. 68–72, January 1963.
7. E. F. Knott, A. W. Reed, and P. S. P. Wei, "Broadside echoes from wires and strings," *Microwave Journal*, pp. 102 *et seq.*, January 1999.
8. S. S. Chang and V. V. Liepa, "Measured backscattering cross section of thin wires, University of Michigan, Rad. Lab. Rept. 8077-4-T, May 1967.
9. L. Peters, Jr., "End-fire echo area of long, thin bodies," *IRE Trans.*, vol. AP-6, pp. 133–139, January 1958.
10. P. S. P. Wei, A. W. Reed, C. N. Ericksen, and M. D. Bushbeck, "Study of RCS measurements from a large flat plate," in *Proc. 27th AMTA Conference, Antenna Measurement Techniques Association Symposium*, Newport, RI, October 31, 2005, pp. 3–8.
11. E. F. Knott, "A tool for predicting the radar cross section of an arbitrary corner reflector," in *IEEE Publ., IEEE Southeastcon '81 Conference*, 81CH1650-1, Huntsville, AL, April 6–8, 1981, pp. 17–20.

12. E. F. Knott, "RCS reduction of dihedral corners," *IEEE Trans.*, vol. AP-25, pp. 406–409, May 1977.
13. W. C. Anderson, "Consequences of non-orthogonality on the scattering properties of dihedral reflectors," *IEEE Trans.*, vol. AP-35, pp. 1154–1159, October 1987.
14. E. F. Knott, J. F. Shaeffer, and M. T. Tuley, *Radar Cross Section*, Raleigh, NC: SciTech Publishing, Inc., 2004, p. 254.
15. R. G. Hajovsky, A. P. Deam, and A. H. LaGrone, "Radar reflections from insects in the lower atmosphere," *IEEE Trans.*, vol. AP-14, pp. 224–227, March 1966.
16. F. V. Schultz, R. C. Burgener, and S. King, "Measurements of the radar cross section of a man," *Proc. IRE*, vol. 46, pp. 476–481, February 1958.
17. C. R. Vaughn, "Birds and insects as radar targets: A review," *Proc. IEEE*, vol. 73, pp. 205–227, February 1985.
18. J. R. Riley, "Radar cross section of insects," *Proc. IEEE*, vol. 73, pp. 228–232, February 1985.
19. L. N. Ridenour (ed.), *Radar System Engineering*, MIT Radiation Laboratory Series, Vol. 1, New York: McGraw-Hill Book Company, 1947, p. 76.
20. U.S. Air Force web site, December 2005, <http://www.wrs.af.mil/other/mmj/compres.htm>.
21. M. I. Skolnik, *Introduction to Radar Systems*, New York: McGraw-Hill Book Company, 1980, p. 45.
22. M. I. Skolnik, "An empirical formula for the radar cross section of ships at grazing incidence," *IEEE Trans.*, vol. AES-10, p. 292, March 1974.
23. S. Ramo and J. R. Whinnery, *Fields and Waves in Modern Radio*, 2nd Ed., New York: John Wiley & Sons, 1960, pp. 272–273.
24. J. A. Stratton, Ref. 4, pp. 464–467.
25. R. F. Harrington, *Field Computation by Moment Methods*, New York: Macmillan Company, 1968.
26. R. E. Kleinman, "The Rayleigh Region," *Proc. IEEE*, vol. 53, pp. 848–856, August 1965.
27. J. W. Crispin, Jr. and K. M. Siegel, eds., *Methods of Radar Cross Section Analysis*, New York: Academic Press, 1968, pp. 144–152.
28. E. F. Knott, "A progression of high-frequency RCS prediction techniques," *Proc. IEEE*, vol. 73, pp. 252–264, February 1985.
29. E. F. Knott et al., Ref. 14, p. 192.
30. E. F. Knott et al., Ref. 14, pp. 194–195.
31. T. B. A. Senior, "A survey of analytical techniques for cross-section estimation," *Proc. IEEE*, vol. 53, pp. 822–833, August 1965.
32. I. J. Gupta and W. D. Burnside, "Physical optics correction for backscattering from curved surfaces," *IEEE Trans.*, vol. AP-35, pp. 553–561, May 1987.
33. J. B. Keller, "Diffraction by an aperture," *J. Appl. Phys.*, vol. 28, pp. 426–444, April 1957.
34. J. B. Keller, "Geometrical theory of diffraction," *J. Opt. Soc. Am.*, vol. 52, pp. 116–130, 1962.
35. R. G. Kouyoumjian and P. H. Pathak, "A uniform theory of diffraction for an edge in a perfectly conducting surface," *Proc. IEEE*, vol. 62, pp. 1448–1461, November 1974.
36. J. J. Bowman, P. L. E. Uslenghi, and T. B. A. Senior (eds.), *Electromagnetic and Acoustic Scattering by Simple Shapes*, Amsterdam: North-Holland, 1969, p. 258.
37. P. Ia. Ufimtsev, "Approximate computation of the diffraction of plane electromagnetic waves at certain metal boundaries, Part I: Diffraction patterns at a wedge and a ribbon," *Zh. Tekhn. Fiz. (U.S.S.R)*, vol. 27, no. 8, pp. 1708–1718, 1957.
38. P. Ia. Ufimtsev, "Approximate computation of the diffraction of plane electromagnetic waves at certain metal boundaries, Part II: The diffraction by a disk and by a finite cylinder," *Zh. Tekhn. Fiz. (U.S.S.R)*, vol. 28, no. 11, pp. 2604–2616, 1958.
39. P. Ia. Ufimtsev, "Method of edge waves in the physical theory of diffraction," U. S. Air Force Systems Command, Foreign Technology Division Doc. FTD-HC-23-259-71, 1971. (Translated from the Russian version published by Moscow: Soviet Radio Publication House, 1962.)

40. E. F. Knott et al., Ref. 14, pp. 209–214.
41. K. M. Mitzner, “Incremental length diffraction coefficients,” Northrop Corporation, Aircraft Div. Tech. Rept. AFAL-TR-73-296, April 1974.
42. E. F. Knott, “The relationship between Mitzner’s ILDC and Michaeli’s equivalent currents,” *IEEE Trans.*, vol. AP-33, pp. 112–114, January 1985. [In the last term of Eq. (15) in this reference, the dot preceding the minus sign should be deleted and β should be replaced by $\sin \beta$; in Eq. (20), the sign of the first term on the right side must be reversed.]
43. A. Michaeli, “Equivalent edge currents for arbitrary aspects of observation,” *IEEE Trans.*, vol. AP-32, pp. 252–258, March 1984. (See also correction, vol. AP-33, p. 227, February 1985.)
44. A. Michaeli, “Elimination of infinities in equivalent edge currents, Part I: Fringe current components,” *IEEE Trans.*, vol. AP-34, pp. 912–918, July 1986.
45. A. Michaeli, “Elimination of infinities in equivalent edge currents, Part II: Physical optics components,” *IEEE Trans.*, vol. AP-34, pp. 1034–1037, August 1986.
46. F. A. Sikta, W. D. Burnside, T. T. Chu, and L. Peters, Jr., “First-order equivalent current and corner diffraction scattering from flat plate structures,” *IEEE Trans.*, vol. AP-31, pp. 584–589, July 1983.
47. R. B. Mack, “Basic design principles of electromagnetic scattering measurement facilities,” Rome Air Development Center Rept. RADC-TR-81-40, March 1981.
48. R. B. Dybdal, “Radar cross section measurements,” *Proc. IEEE*, vol. 75, pp. 498–516, April 1987.
49. R. G. Kouyoumjian and L. Peters, Jr., “Range requirements in radar cross section measurements,” *Proc. IEEE*, vol. 53, pp. 920–928, August 1965.
50. E. F. Knott et al., Ref. 14, p. 461.
51. M. A. Plonus, “Theoretical investigation of scattering from plastic foams,” *IEEE Trans.*, vol. AP-13, pp. 88–93, January 1965.
52. T. B. A. Senior, M. A. Plonus, and E. F. Knott, “Designing foamed-plastic materials,” *Microwaves*, pp. 38–43, December 1964.
53. E. F. Knott and T. B. A. Senior, “Studies of scattering by cellular plastic materials,” University of Michigan, Rad. Lab. Rept. 5849-1-F, April 1964.
54. C. C. Freeny, “Target support parameters associated with radar reflectivity measurements,” *Proc. IEEE*, vol. 53, pp. 929–936, August 1965.
55. E. F. Knott et al., Ref. 14, p. 471.
56. W. H. Emerson, “Electromagnetic wave absorbers and anechoic chambers through the years,” *IEEE Trans.*, vol. AP-21, pp. 484–490, July 1973.
57. L. Solomon, “Radar cross section measurements: How accurate are they?” *Electronics*, vol. 35, pp. 48–52, July 20, 1962.
58. W. H. Emerson and H. B. Sefton, Jr., “An improved design for indoor ranges,” *Proc. IEEE*, vol. 53, pp. 1079–1081, August 1965.
59. H. E. King, F. I. Shimabukuro, and J. L. Wong, “Characteristics of a tapered anechoic chamber,” *IEEE Trans.*, vol. AP-15, pp. 488–490, May 1967.
60. R. B. Dybdal and C. O. Yowell, “VHF to EHF performance of a 90-foot quasi-tapered anechoic chamber,” *IEEE Trans.*, vol. AP-21, pp. 579–581, July 1973.
61. R. C. Johnson, H. A. Ecker, and R. A. Moore, “Compact range techniques and measurements,” *IEEE Trans.*, vol. AP-17, pp. 568–576, September 1969.
62. W. D. Burnside, M. C. Gilreath, B. M. Kent, and G. L. Clerici, “Curved edge modification of compact range reflector,” *IEEE Trans.*, vol. AP-35, pp. 176–182, February 1987.
63. R. C. Rudduck, M. C. Liang, W. D. Burnside, and J. S. Yu, “Feasibility of compact ranges for near-zone measurements,” *IEEE Trans.*, vol. AP-35, pp. 280–286, March 1987.
64. W. D. Burnside, C. W. Pistorius, and M. C. Gilreath, “A dual chamber Gregorian subreflector for compact range applications,” *Proc. of the Antenna Measurement Techniques Association*, September 28–October 2, 1987, pp. 90–94.

65. E. F. Knott, *Radar Cross Section Measurements*, New York: Van Nostrand Reinhold, 1993, pp. 33–38.
66. D. L. Mensa, *High Resolution Radar Imaging*, Norwood, MA: Artech House, 1981.
67. W. W. Salisbury, “Absorbent Body for Electromagnetic Waves,” U.S. Patent 2,599,944, June 10, 1952.
68. W. E. Blore, “The radar cross section of ogives, double-backed cones, double rounded cones, and cone spheres,” *IEEE Trans.*, vol. AP-12, pp. 582–590, September 1964.
69. M. D. O’Leary and Eric Schulzinger, *SR-71: Inside Lockheed’s Blackbird*, Oseola, WI: Motorbooks International Publishers & Wholesalers, 1991.
70. B. Sweetman and J. Goodall, *Lockheed F-117A*, Oseola, WI: Motorbooks International Publishers & Wholesalers, 1990.
71. E. F. Knott, “RCSR Guidelines Handbook,” Final Technical Report on EES/GIT Project A-1560-001,” Engineering Experiment Station, Georgia Institute of Technology, April 1976.